

# Dispersive readout scheme for a Josephson phase qubit

Zur Erlangung des akademischen Grades eines  
DOKTORS DER NATURWISSENSCHAFTEN  
von der Fakultät für Physik des  
Karlsruher Instituts für Technologie (KIT)

genehmigte

DISSERTATION

von

Dipl.-Phys. Tobias Wirth  
aus Nürnberg

Tag der mündlichen Prüfung: 15. April 2011

Referent: Prof. Dr. Alexey V. Ustinov

Koreferent: Prof. Dr. Georg Weiß



# Contents

<b>1</b>	<b>Introduction</b>	<b>1</b>
<b>2</b>	<b>The Josephson Phase Qubit</b>	<b>5</b>
2.1	A single Josephson junction . . . . .	5
2.2	Superconducting quantum interference devices . . . . .	10
2.2.1	The rf-SQUID . . . . .	11
2.2.2	The dc-SQUID . . . . .	15
2.3	The flux biased phase qubit system . . . . .	17
2.3.1	Qubit operation cycle . . . . .	20
2.3.2	Rabi oscillations . . . . .	20
<b>3</b>	<b>Dispersive readout scheme of the SQUID resonator</b>	<b>27</b>
3.1	SQUID-resonator in the linear regime . . . . .	28
3.2	SQUID-resonator in the non-linear regime . . . . .	32
<b>4</b>	<b>Experimental Technique</b>	<b>35</b>
4.1	Sample design and fabrication . . . . .	35
4.2	LTLSM setup . . . . .	36
4.3	Switching current measurement setup . . . . .	44
4.3.1	Wiring and filtering . . . . .	45
4.3.2	Electronics . . . . .	46
4.4	Measurement setup for dispersive readout . . . . .	50
4.4.1	DC electronics . . . . .	51
4.4.2	Microwave electronics setup . . . . .	51

*Contents*

---

<b>5 Measurement Results</b>	<b>63</b>
5.1 LTLSM Measurements . . . . .	63
5.2 Switching current measurements . . . . .	71
5.3 Measurements on the dispersive readout . . . . .	73
5.3.1 SQUID detector characterization . . . . .	74
5.3.2 Qubit readout . . . . .	82
<b>Conclusions</b>	<b>85</b>
<b>Bibliography</b>	<b>92</b>
<b>List of publications</b>	<b>93</b>
<b>Acknowledgements</b>	<b>95</b>

# Chapter 1

## Introduction

This thesis is devoted to experimental studies on the dispersive readout of a superconducting quantum interference device (SQUID) which is used to detect the state of a quantum bit (qubit). Superconducting circuits are one of a number of possible technologies for storing and processing data in quantum computers. Superconducting qubits offer the advantage of being manufactured using standard micro fabrication technologies and can be easily interconnected to larger qubit circuits. The success story of superconducting qubits started in 1999, when Nakamura et al. [NPT99] showed quantum coherence of a macroscopic system in experiments on charge qubits. This pioneering discovery led to a rapid development of various approaches to superconducting qubits, nowadays reaching coherence times up to microseconds. However, coupling to the environment, including controlling wires as well as the substrate material, leads to shorter coherence times. Studies of sources of decoherence form a major part of recent research.

A vital ingredient of experiments on quantum bits is a detection tool to efficiently read out the state of a qubit. This detector must introduce as little back-action as possible, while showing a large measurement contrast; it should have negligible dissipation and offer fast operation. Superconducting quantum bits, such as the flux [MOL<sup>+</sup>99] and phase qubit [MNAU02a], consist of superconducting loops interrupted by one or more Josephson junctions. Since their readable states can be discriminated by the magnetic flux passing through the qubit loop, it is common to use inductively coupled dc-SQUIDs

as sensitive detectors.

The standard method to measure magnetic flux is to record the dc bias current at which the SQUID switches to its non-superconducting state [CSM<sup>+</sup>04, PDP<sup>+</sup>06, CFHB07, LLA<sup>+</sup>07]. This process generates heat directly on the chip and quasi-particles in the circuitry. Both effects are responsible for a relatively long cool-down time of about 1-2 ms after each switching event. Together with the time needed to ramp up the bias current of the SQUID, this limits the repetition rate of the experiment.

For the flux qubit, non-destructive dispersive readout schemes were implemented in the past by coupling either to a high-quality LC-resonator [IOI<sup>+</sup>03] or to a dc-SQUID [LmcVS<sup>+</sup>04]. So far, most measurements of phase qubits have been performed typically by the switching current measurement of an inductively coupled dc-SQUID. Recently, an experiment overcoming the limitations of the switching readout was reported [SKD<sup>+</sup>10]. In that approach, the phase qubit was capacitively coupled to a transmission line which allows for direct probing of its resonance frequency with a microwave pulse. This eliminates a readout dc-SQUID, but introduces decoherence via the line coupled directly to the qubit.

In this thesis, we present experiments on the dispersive readout of a dc-SQUID resonator coupled to a phase qubit. The flux dependent non-linear Josephson inductance of the SQUID, together with a shunt capacitor forms a resonator circuit which in turn has a flux dependent resonance frequency around 2 GHz. The flux state of the qubit is detected by measuring the amplitude and phase of a microwave pulse reflected from the SQUID resonator. By this low-dissipative method, the qubit state measurement time is reduced to 25  $\mu$ s, which is much faster than the conventional readout performed by switching the SQUID to its non-zero dc voltage state.

By using weak coupling between the SQUID and the qubit, this scheme protects the qubit from decoherence sources introduced by the readout circuitry. Moreover, while preserving the intrinsic coherence of the qubit, this method is suitable for reading out many qubits using a single microwave line and frequency-division multiplexing to address individual readout SQUID resonators.

In chapter 2 of this thesis, the physics of small Josephson junctions is

---

briefly introduced. It involves quantum interference of a macroscopic observable in superconducting loops containing Josephson junctions. Since we make use of SQUIDs with one and more junctions enclosed in the loop, the characteristics of these devices are discussed. We describe the phase qubit system which consists of an rf-SQUID, a dc-SQUID and a flux line. A description of coherent oscillations in a single qubit concludes the second chapter.

A more detailed description of the dispersive readout scheme of the SQUID resonator is given in chapter 3. The Josephson inductance of the SQUID is introduced and it is explained how to yield the desired resonance frequency of the system. This chapter concludes with a brief introduction of the non-linear regime, the resonator can enter under strong microwave drive.

Chapter 4 gives an overview on how the experiments were done. It provides a brief description of the sample design and their fabrication. The low temperature laser scanning microscope (LTLSM) and its measurement technique is introduced. We describe the different measurement setups that are used in our dilution refrigerator and at room temperature respectively, to perform the switching readout of the phase qubit on the one hand, and the dispersive readout on the other hand.

Chapter 5 is dedicated to the experimental results, starting from the measurements of resonators performed with the LTLSM. The measurements involving the switching readout of the qubit are briefly discussed. The last section presents the measurements on the dispersive readout scheme of the phase qubit, starting with the characterization of the SQUID detector in the frequency domain by means of a vector network analyzer (VNA). Comparative measurements in the frequency domain involving a custom made microwave board instead of the VNA are shown. Using this board, fast measurements in the time domain were performed, revealing coherent oscillations between the qubit states.

The thesis ends with a brief summary of the obtained results.



# Chapter 2

## The Josephson Phase Qubit

### 2.1 A single Josephson junction

A Josephson junction is based on the phenomenon of superconductivity, which was discovered in 1911 at the Leiden Laboratory by Heike Kamerlingh Onnes while measuring the temperature dependence of the electrical resistance of mercury [KO11]. Kamerlingh Onnes noticed the resistance of the sample dropping to zero when cooled down to about 4K.

In 1957, the BCS-theory, named after the authors John Bardeen, Leon Neil Cooper and John Robert Schrieffer, was published [BCS57]. According to their theory, conduction electrons of opposite momenta and spins form bound pairs under the influence of phonon induced attraction. A so-called Cooper pair has zero spin and is therefore subject to Bose-Einstein statistics. At low temperatures, these Cooper pairs condense into the lowest energy state (the ground state), in some respect similar to a Bose condensate. At finite temperatures, thermal fluctuations break some of the Cooper pairs, creating normal electrons. Because of the presence of superconductivity, these electrons have different properties compared to normal-metal electrons and are therefore called quasiparticles. The quasiparticle states are separated from the ground state by a gap  $\Delta$  which is proportional to the binding energy of a Cooper pair. Since the size of a Cooper pair is larger than the mean spacing between the pairs by three orders of magnitude [Lik86], the wave functions of the Cooper pairs are overlapping. The resulting superconducting

condensate can be described by a single wave function

$$\Psi = |\Psi_0(\vec{x}, t)| \exp \{i\phi(\vec{x}, t)\}, \quad (2.1)$$

also called the order parameter. Here  $|\Psi_0|^2$  is proportional to the density of Cooper pairs and  $\phi(\vec{x}, t)$  is the phase of the wavefunction. The current in a superconductor is formed by coherent motion of a macroscopic number of Cooper pairs.

While the amplitude  $|\Psi|^2$  of the order parameter is constant inside the superconductor, it extends beyond its physical (material) dimensions where it decays exponentially. This allows an overlap of the wavefunctions of two superconductors separated by a weak link and hence provides a coupling between them, see Fig. 2.1.

Let us consider now two superconductors coupled by a weak link as shown in Fig. 2.1. In 1962, Brian D. Josephson published his remarkable theory [Jos62] about such systems of weakly coupled superconductors, which later were called Josephson junctions. At room temperature, a Josephson junction behaves as an Ohmic resistance  $R_n$  of a few Ohm. Once superconducting, the insulating barrier is penetrated by the wavefunctions of both superconductors. These wavefunctions overlap as shown in the lower part of Fig. 2.1 and allow a certain current of Cooper pairs to flow without resistance. Josephson predicted that this supercurrent depends only on the difference

$$\varphi = \phi_2 - \phi_1, \quad (2.2)$$

between the phases of the wavefunctions in both superconductors. This phase difference is also called Josephson phase and obeys the first Josephson equation

$$I_b = I_c \sin \varphi, \quad (2.3)$$

which describes the dc Josephson effect, where  $I_c$  is the maximum dissipationless current which can flow through the junction, also called critical

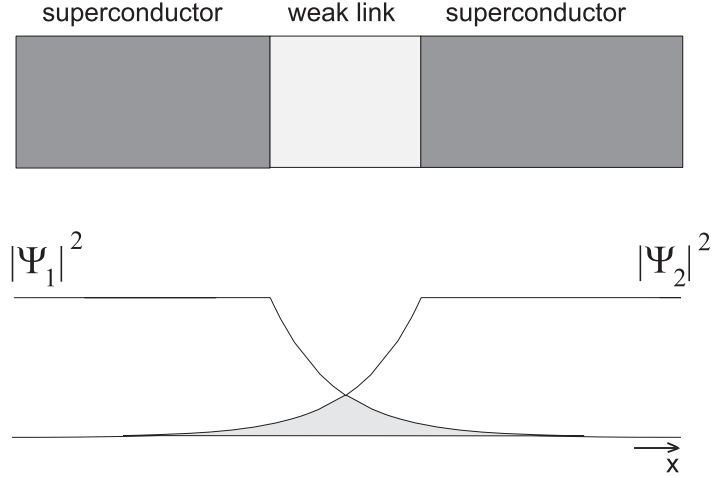


**Figure 2.1:** At the boundary of a superconductor, the amplitude of the order parameter decays exponentially, as shown in the lower part of the picture. This allows an overlap (shaded grey) of the two wavefunctions and provides a coupling between them.

current.  $I_c$  is specific for a junction and depends on the electrode material, the normal resistance of the tunnel barrier and the temperature [AB63]. As long as the amplitude of a constant current  $I_b$  flowing through the barrier does not exceed the critical current  $I_c$ , there is no voltage drop across the junction, and the Josephson phase according to Eq. (2.3) will be constant,  $\varphi = \arcsin(\frac{I_b}{I_c} + 2\pi n)$ .

If the junction is biased with a current  $I_b > I_c$ , it will become resistive and dissipation occurs. In this case a voltage drop  $V > 0$  across the junction is induced by an additional tunneling current of normal electrons.

In this case, the second fundamental equation relates the voltage drop  $V$  across the junction to the time evolution of the phase difference  $\varphi$ :

$$V = \frac{\Phi_0}{2\pi} \frac{d\varphi}{dt}, \quad (2.4)$$

where  $\Phi_0$  is the flux quantum  $\Phi_0 = \frac{h}{2e} = 2.07 \cdot 10^{-15} \text{Vs}$ ,  $e$  is the electron

charge  $e = 1.6022 \cdot 10^{-19} \text{As}$  and  $h$  is Planck's constant  $h = 6.626 \cdot 10^{-34} \text{VAs}^2$ . Equation (2.4) is called second Josephson equation. An instructive derivation of both Josephson equations can be found in [FLS94].

By integration of Eq. (2.4) follows that  $\varphi = \frac{2\pi}{\Phi_0} Vt + \varphi_0$ . Combining Eqs. (2.3) and (2.4) implies that a constant voltage applied to the junction results in an alternating current,

$$I = I_c \sin\left(\frac{2\pi}{\Phi_0} Vt + \varphi_0\right) = I_c \sin(\omega_J t + \varphi_0), \quad (2.5)$$

where the oscillation frequency is given by

$$\nu_J = \frac{\omega_J}{2\pi} = \frac{V}{\Phi_0}, \quad (2.6)$$

which is called Josephson frequency. The appearance of the ac current is the ac Josephson effect. The conversion ratio between voltage and frequency, according to Eq. (2.6), is known very precisely through the fundamental constants  $e$  and  $h$ :

$$\frac{\nu_J}{V} = \frac{1}{\Phi_0} = \frac{2e}{h} = 483.59767 \frac{\text{MHz}}{\mu\text{V}}. \quad (2.7)$$

Hence any voltage  $V > 0$  across the junction is converted to an oscillating current and vice versa, a change in the supercurrent respectively Josephson phase will result in a nonzero voltage. The junction thus acts like a non-linear inductance. By combining the general current-voltage relation of an inductance  $V = L \frac{dI}{dt}$  with the two Josephson relations, Eqs. (2.3) and (2.4) one can obtain the Josephson inductance

$$L_J(\varphi) = \frac{\Phi_0}{2\pi I_c} \frac{1}{\cos \varphi} = L_J(0) \frac{1}{\cos \varphi}, \quad (2.8)$$

where

$$L_J(0) = \frac{\Phi_0}{2\pi I_c}, \quad (2.9)$$

is the Josephson inductance for the Josephson phase  $\varphi = 0$ .

One should be aware of the fact that the Josephson inductance given by Eq. (2.8) is time dependent, following the changes of the Josephson phase  $\varphi$  and can also take negative values.

The total current flowing in a Josephson junction consists of two parts, due to the presence of superconducting and normal electrons. Stewart [Ste68] and McCumber [McC68] introduced the resistively and capacitively shunted junction model (RCSJ - model) which applies to small junctions, with dimensions smaller than the characteristic length of variations in the Josephson phase  $\varphi$  across the junction. They considered the Josephson junction as a parallel combination of an ohmic resistor  $R$ , which represents its effective shunt resistance, the Josephson supercurrent element, which behaves according to Eq. (2.3) and a capacitor  $C$ , accounting for the total capacitance of the electrodes.

According to Kirchhoff's law, the total current  $I$  flowing through this circuit is the sum of the currents in each of the three branches. Using Eq. (2.4), leads to:

$$I = I_c \sin \varphi + \frac{V}{R} + C \frac{dV}{dt} = I_c \sin \varphi + \frac{1}{R} \frac{\Phi_0}{2\pi} \dot{\varphi} + C \frac{\Phi_0}{2\pi} \ddot{\varphi}. \quad (2.10)$$

We can rewrite Eq. (2.10) as an equation of motion,

$$m\ddot{\varphi} + m \frac{1}{RC} \dot{\varphi} + \frac{\Phi_0}{2\pi} (I_c \sin \varphi - I) = 0, \quad (2.11)$$

or

$$m\ddot{\varphi} + m \frac{1}{RC} \dot{\varphi} + \frac{\partial U(\varphi)}{\partial \varphi} = 0 \quad (2.12)$$

for a virtual particle of mass  $m = C(\Phi_0/2\pi)^2$  moving along its generalized coordinate  $\varphi$  in a potential  $U(\varphi)$ . The potential is given by

$$U(\varphi) = \frac{I_c \Phi_0}{2\pi} \left( -\frac{I}{I_c} \varphi - \cos \varphi \right) = E_J (-\gamma \varphi - \cos \varphi), \quad (2.13)$$

where  $\gamma = I/I_c$  is the normalized bias current and  $E_J$  is the Josephson energy,

$$E_J = \frac{I_c \Phi_0}{2\pi}. \quad (2.14)$$

Put together with the effective inductance  $L$  of the junction, given by Eq. (2.8), the capacitance  $C$  of the barrier gives rise to an oscillation of the voltage across the junction at the characteristic frequency

$$\nu_0 = \frac{\omega_0}{2\pi} = \frac{1}{2\pi\sqrt{LC}} = \nu_p(\cos \varphi)^{1/2}, \quad (2.15)$$

where  $\nu_p$  is the Josephson plasma frequency,

$$\nu_p = \frac{\omega_p}{2\pi} = \frac{1}{2\pi} \left( \frac{2\pi I_c}{\Phi_0 C} \right)^{1/2}. \quad (2.16)$$

In terms of the normalized bias current  $\gamma$ , the characteristic frequency can be written as

$$\nu_0 = \nu_p(1 - \gamma^2)^{1/4}. \quad (2.17)$$

A Josephson tunnel junction can be viewed as a nonlinear oscillator, whose characteristic time scale is determined by the plasma frequency. For typical tunnel junctions,  $\nu_p$  is in the microwave range of several tens of GHz.

## 2.2 Superconducting quantum interference devices

This section is dedicated to the devices known as superconducting quantum interferometers. These devices, though very simple in design, have opened new horizons in low temperature measurement techniques providing new tools to measure extremely small magnetic fields, and moreover are the basis of many solid state qubits. A further and more detailed discussion of SQUIDs and their applications can be found in [CB04].

### 2.2.1 A Josephson junction in a superconducting loop

In this section we describe the rf-SQUID, which consists of a Josephson junction enclosed in a superconducting loop, see Fig. 2.2.

When an external magnetic field is applied to the loop, a screening current  $I_{\text{circ}}$  circulates in the ring. This screening current produces a magnetic flux  $L_{\text{self}}I_{\text{circ}}$ , which changes the external flux. The resulting flux is given by

$$\Phi = \Phi_{\text{ext}} - L_{\text{self}}I_{\text{circ}}, \quad (2.18)$$

where  $L_{\text{self}}$  is the self inductance of the loop. The circulating current obeys the first Josephson equation (2.3) and is therefore:

$$I_{\text{circ}} = I_c \sin \varphi. \quad (2.19)$$

By combining Eqs. (2.18) and (2.19) and the phase-flux-relation

$$\varphi = \frac{2\pi}{\Phi_0} \Phi, \quad (2.20)$$

we obtain the following equation,

$$\Phi = \Phi_{\text{ext}} - L_{\text{self}}I_c \sin \left( \frac{2\pi}{\Phi_0} \Phi \right), \quad (2.21)$$

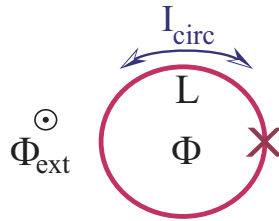


**Figure 2.2:** A superconducting loop with a Josephson junction, which is exposed to the external flux  $\Phi_{\text{ext}}$ . A circulating current is generated which leads to a resulting flux  $\Phi$  inside the loop.

which relates the resulting flux inside the loop  $\Phi$  to the externally applied flux  $\Phi_{\text{ext}}$ . Figure 2.3 shows this relation, plotted for different values of  $L_{\text{self}} I_c$ . We also marked the flux jumps which occur due to the change of the external flux and are periodic with respect to a change of  $\Phi_0$  in the loop. These flux jumps are essential for the use of the rf-SQUID as an qubit, as will be explained later in this chapter.

The potential energy of a single Josephson junction is already known from section 2.1, Eq. (2.13). By adding the magnetic energy of a loop, one obtains the potential energy of the rf-SQUID:

$$U_{\text{rf-SQUID}} = E_J(1 - \cos \varphi) + \underbrace{\frac{1}{2} L_{\text{self}} (I_{\text{circ}})^2}_{\text{magnetic energy}} . \quad (2.22)$$

Using equation (2.18) and (2.20), the potential energy of the rf-SQUID is

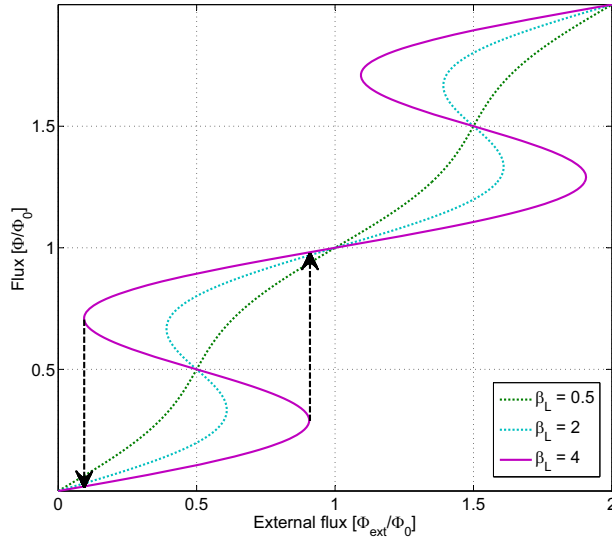


**Figure 2.3:** Resulting flux in the rf-SQUID  $\Phi$  versus externally applied flux  $\Phi_{\text{ext}}$ . Arrows mark the flux jumps.

## 2.2. Superconducting quantum interference devices

---

expressed as,

$$U_{\text{rf-SQUID}} = E_J \left[ 1 - \cos \varphi + \frac{(\varphi - \frac{2\pi}{\Phi_0} \Phi_{\text{ext}})^2}{2\beta_L} \right], \quad (2.23)$$

where

$$\beta_L = \frac{2\pi L_{\text{self}} I_c}{\Phi_0} \quad (2.24)$$

is the self-inductance parameter, which is proportional to  $I_c$  and  $L_{\text{self}}$ , the two design parameters of the rf-SQUID. Thus, the dynamics of the rf-SQUID can be visualized as motion of a virtual particle in a one-dimensional potential, as shown in Fig. 2.4 and in Fig. 2.5.

At low temperatures the classical analog, which describes a particle oscillating in the potential, is no longer useful for an appropriate description of the phase dynamics because the quantization of the energy of the phase becomes relevant. This was experimentally observed for the first time in the pioneering work of John Martinis, Michel Devoret and John Clarke [MDC85] using microwave activation.

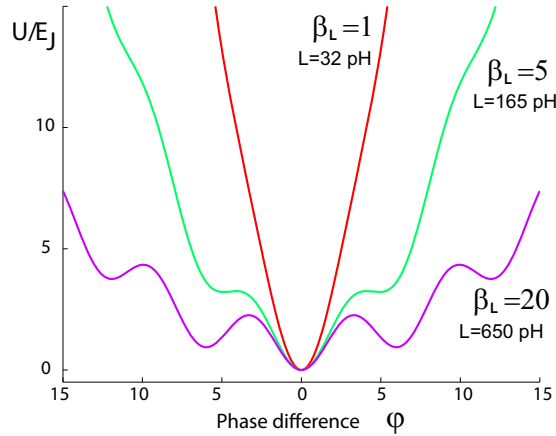


**Figure 2.4:** Potential energy of an rf-SQUID, plotted for  $\Phi_{\text{ext}} = 0$  and different values of  $\beta_L$ . The corresponding self-inductances are also denoted for a critical current  $I_c = 10 \mu\text{A}$ . The energy scale is normalized to the Josephson energy  $E_J$ .

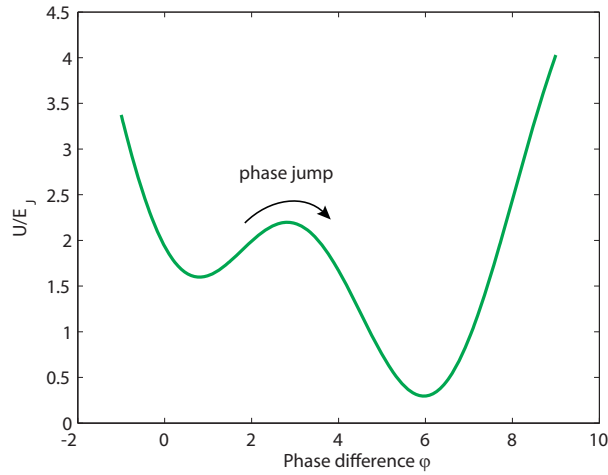


**Figure 2.5:** Potential energy of an rf-SQUID, plotted for  $\beta_L = 5$  and  $\Phi_{\text{ext}} = 0.7 \Phi_0$ . Biasing the rf-SQUID at  $\Phi_{\text{ext}} \approx \Phi_0$ , leads to a double well potential with a shallow left and a deep right well. The arrow denotes a phase jump of the virtual particle.

The positions of the energy levels may be estimated by a harmonic approximation to one potential well, see Figure 2.6.

For a quadratic potential, the energy of the ground state is given by

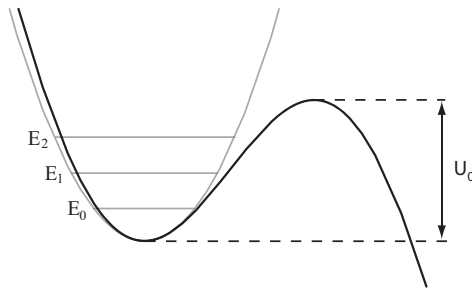


**Figure 2.6:** Harmonic approximation to one metastable well and the corresponding discrete and equidistant energy levels.  $U_0$  is the height of the potential barrier.

$E_0 = \hbar\omega_0/2$ , while the excited states satisfy

$$E_n = \left(n + \frac{1}{2}\right) \hbar\omega_0, \quad (2.25)$$

where  $n$  is the quantum number of the state. In reality, the potential is not harmonic, and this has the consequence that the spacing between adjacent levels decreases with increasing energy. Increasing the bias current implies according to Eqs. (2.15) and (2.16), that all levels move closer together, while upper levels drop out of the well due to the decrease of the barrier height  $U_0$ . A rough estimate for the number of levels  $N$  in the well is

$$N \approx \frac{U_0}{\hbar\omega_0}. \quad (2.26)$$

### 2.2.2 The dc-SQUID

As the rf-SQUID, a dc-SQUID basically consists of a superconducting loop, but interrupted by more than one Josephson junctions, as seen in the left part of Fig. 2.7. Let us assume a symmetric configuration, both junctions are identical, have the same critical current  $I_c$  and therefore the same Josephson inductance  $L_J$ . The self inductance of the loop  $L_{\text{self}}$  is neglected for the moment.

An externally applied magnetic field gives rise to a circulating current as in the rf-SQUID. This current  $I$  splits equally to both branches of the ring. Following the derivation in [Sch97], we find that the maximum critical current of the dc-SQUID is determined by

$$I_{c,\text{SQUID}}(\Phi) = 2I_{c0} \left| \cos\left(\frac{\pi\Phi}{\Phi_0}\right) \right|, \quad (2.27)$$

where  $I_{c0}$  is the critical current of a single junction in the SQUID. Figure 2.8 shows the dependence of the critical current of the dc-SQUID on the externally applied magnetic flux.

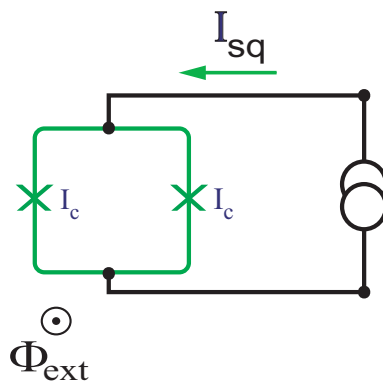


**Figure 2.7:** A symmetric dc-SQUID (green) with two identical junctions. The SQUID is connected to a current source, which biases the SQUID at  $I_{sq}$ .

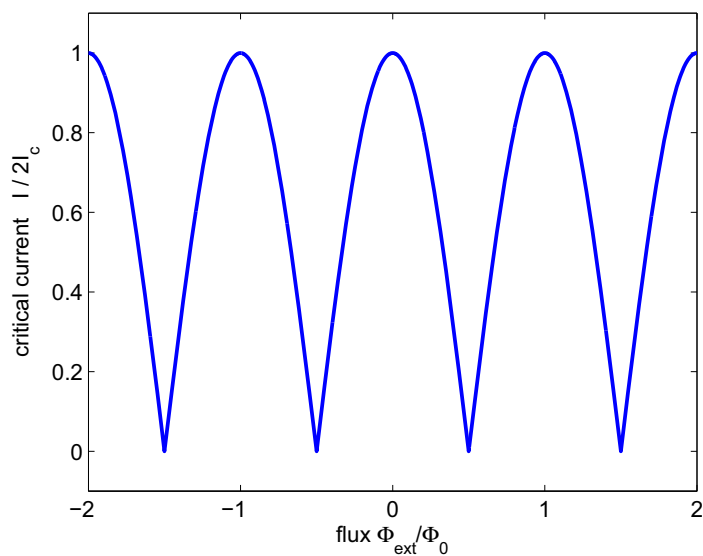


**Figure 2.8:** Dependence of the critical current of a dc-SQUID on the externally applied magnetic flux.

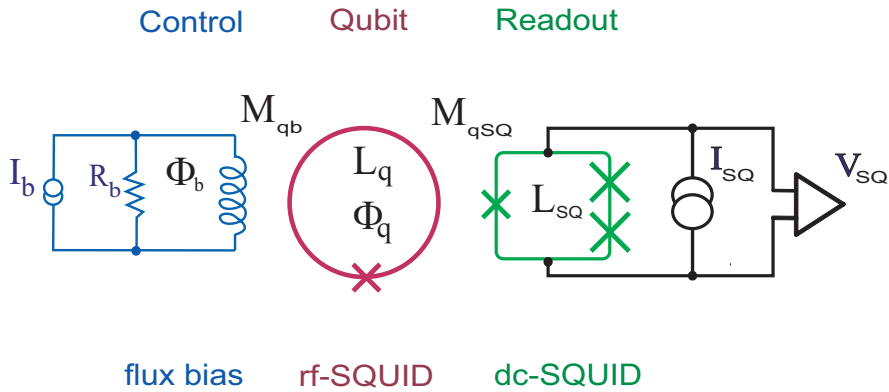
## 2.3 The flux biased phase qubit system

Current-biased large Josephson junctions have been recently proposed and realized as Josephson phase qubits, see [MNAU02b], [YHC<sup>+</sup>02] and [BXR<sup>+</sup>03]. To galvanically decouple the qubit from the environment, a superconducting transformer has been introduced. Figure 2.9 shows a model of such a qubit system. The rf-SQUID in the middle is the qubit itself. A dc-SQUID, which is inductively coupled to the rf-SQUID, is used to read out the qubit states. A current source connected to a flux line, which is inductively coupled to the system, is used to bias the rf-SQUID.

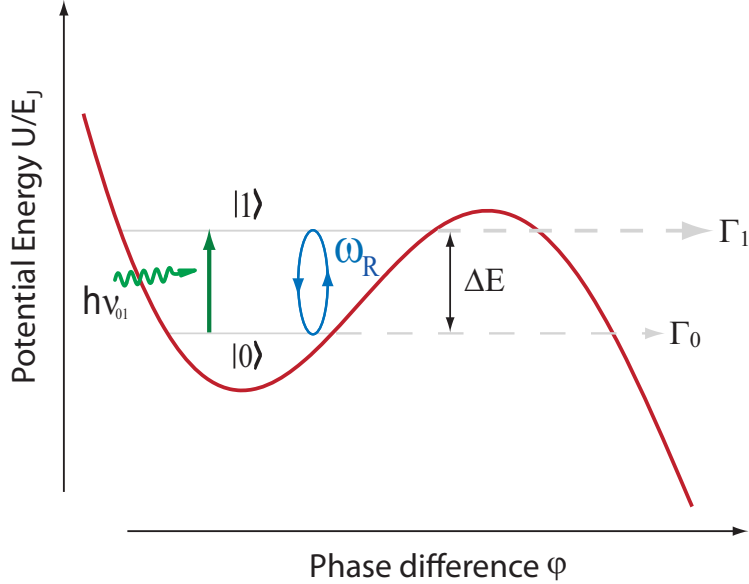
When biased at a flux  $\Phi \approx \Phi_0$ , the system is described by a double well potential in the phase coordinate, with one shallow and one deep potential well, as shown in Fig. 2.5.

Figure 2.10 shows the shallow well of this potential. In the quantum picture the state of the Josephson phase is described by its quantized energy levels. The lowest energy levels remaining in the anharmonic shallow potential well can be treated as a two level quantum system, usable as a qubit. The qubit states  $|0\rangle$  and  $|1\rangle$  are represented by the phase ground and first excited state, respectively.

For a single shot read-out of the quantum state, a short flux pulse is applied to the rf-SQUID by increasing the bias current of the flux line for



**Figure 2.9:** Qubit system, which consists of the flux bias, the rf-SQUID and the dc-SQUID.



**Figure 2.10:** Quantum picture of the states of the Josephson phase inside the shallow well, wherein the discrete energy levels are indicated as grey horizontal lines. Tunneling from the excited state  $|1\rangle$  happens at a rate  $\Gamma_1$ , which is about 1000 times larger than the tunnel rate  $\Gamma_0$  from the ground state  $|0\rangle$ , since the corresponding barrier height is reduced by the energy difference  $\Delta E$ . The green arrow illustrates the resonant activation of the phase from the ground state to the first excited state by absorbing a photon, if the photon energy  $h\nu_{01}$  is equal to the energy difference  $\Delta E$ . The blue cyclic arrow indicates coherent oscillations between the eigenstates of the two-level quantum system which is subject to a continuous resonant perturbation. These so-called Rabi oscillations with a frequency  $\nu_R = \omega_R/2\pi$  will be illustrated in more detail later in this section.

a short period of time. This corresponds to an additional tilt of the double well potential that decreases the potential barrier height and increases the escape rate exponentially. Figure 2.11 illustrates the situation for a flux-pulse-induced potential tilt leading to a reduction of the potential barrier height. In the case that state  $|1\rangle$  is occupied, the phase tunnels to the right well. This effectively maps the states  $|0\rangle$  and  $|1\rangle$  to macroscopically distinct states of magnetic flux in the qubit loop. These flux changes in the qubit loop

are detected by a SQUID (Superconducting Quantum Interference Device) magnetometer which is coupled by a mutual inductance to the qubit.

A crucial point about the dc-SQUID is the coupling to the rf-SQUID. The flux states of the rf-SQUID are mapped to the switching current of the dc-SQUID. For a single-shot readout with a flux pulse, one yields to have a large change in the switching current between the two states. The change in the switching current is given by

$$\Delta I_{\text{SQUID}} = M \cdot \Delta I_q \cdot \frac{\partial I_{\text{SQUID}}}{\partial \Phi_{\text{ext}}}, \quad (2.28)$$

where  $M$  is the mutual inductance between the rf-SQUID and the dc-SQUID loop and  $\Delta I_q$  is the change in circulating current in the rf-SQUID.

The sensitivity of the dc-SQUID can be increased by choosing a working point of the dc-SQUID where  $\partial I_{\text{SQUID}}/\partial \Phi_{\text{ext}}$  is large, as on the slopes of the pattern shown in Fig. 2.8. This can be done, even for  $\Phi_{\text{ext}} = 0$ , by using an asymmetric SQUID. [Lis08], [Wir06]

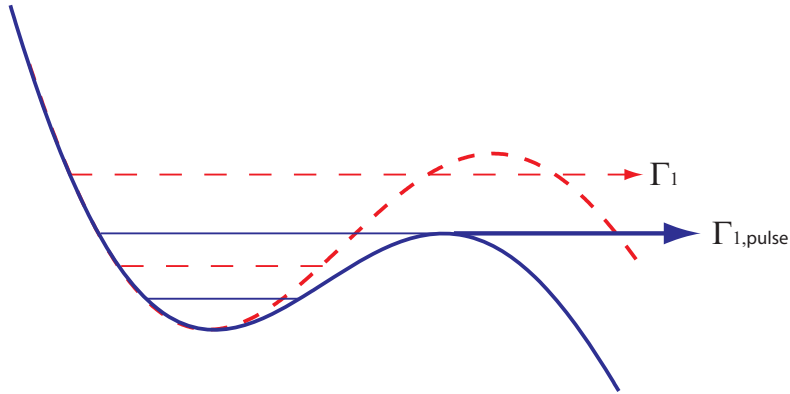


**Figure 2.11:** Schematic drawing of a metastable well with its two lowest energy levels. Drawn in dashed red lines is the situation at normal biasing, in solid blue lines the potential is additionally tilted by a flux pulse. The solid arrow indicates the immediate escape from the excited level due to a very small remaining potential barrier.

### 2.3.1 Qubit operation cycle

Figure 2.12 shows a complete operation cycle of the qubit system. One cycle consists of three basic steps: Qubit initialization, the operation of the qubit itself and finally freezing of the qubit state. During the latter part, the readout is being done.

**Qubit initialization:** Figure 2.12(a) shows that in the beginning a negative flux  $\Phi_{\text{ext}}$  is applied to the system. This tilts the rf-SQUID potential so that only a single deep well exists, as shown by the blue potential curve in Fig. 2.13, and all phase eigenstates are located in this well.

The external flux is then increased to reach a value of  $\Phi_{\text{ext}} \approx \Phi_0$ , where the potential has the shape of the red curve in Fig. 2.13 and only the two lowest phase eigenstates remain in the shallow well. This quantum two level system is now usable as a qubit. The qubit states  $|0\rangle$  and  $|1\rangle$  are represented by the phase ground and first excited state, respectively.

**Qubit operation:** Now a microwave pulse (green) is used to control the state of the qubit. In the picture of the quantum two level system, this microwave current is a resonant perturbation, which leads to a coupling of the two levels. The coupling gives rise to coherent oscillations between the eigenstates of the system.

For a single-shot state readout, a short flux pulse is applied, moving the state  $|1\rangle$  close to the top of the well, see Fig. 2.11. In the case that state  $|1\rangle$  is occupied, the phase tunnels to the right well. This phase jump changes the flux in the qubit loop according to Eq. (2.20) as shown in Fig. 2.3. This effectively maps the states  $|0\rangle$  and  $|1\rangle$  to macroscopically distinct states of magnetic flux in the qubit loop.

**Freezing and readout:** To avoid further tunneling, the potential is tilted back a little by reducing the external flux.

### 2.3.2 Rabi oscillations

Rabi oscillations describe the coherent oscillations between the eigenstates of a quantum two level system, which is subject to a resonant perturbation. They are named after Isidor Isaac Rabi, who was awarded the Nobel Prize

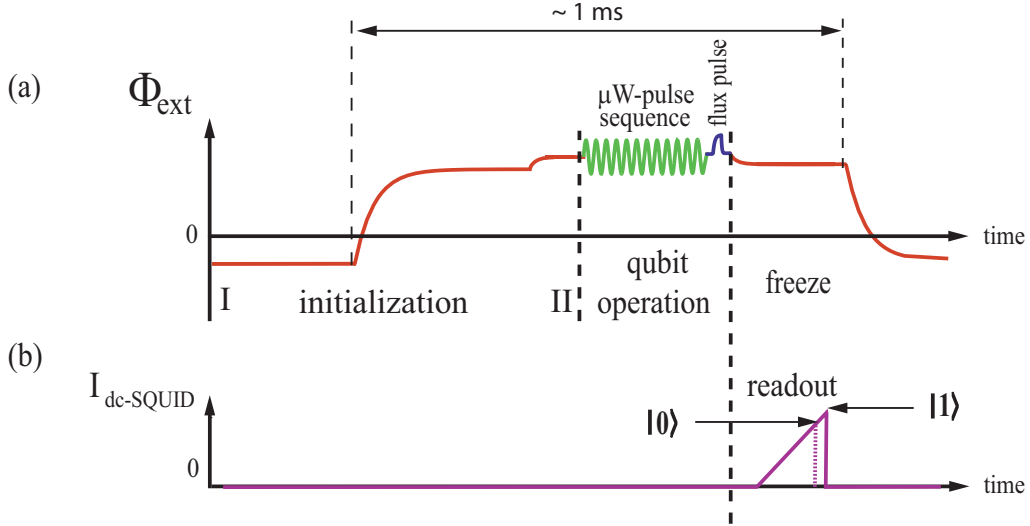


**Figure 2.12:** One operation cycle of the qubit system. The red line shows the time dependence of the flux which is applied to the qubit (a). The violet line shows the time dependence of the bias current of the dc-SQUID (b). The vertical dashed lines divide the whole cycle into three parts which are explained in the text. The time line is not to scale.

for Physics in 1944 for his work on the magnetic properties of atomic nuclei. These oscillations create a superposition of the two states and are therefore crucial for any two level system which should work as a qubit. In our case the oscillations occur between the two phase eigenstates and are induced by a microwave current as the resonant perturbation.

The derivation of the Rabi frequency and the amplitude of the oscillations is a standard problem which is discussed in many books on quantum mechanics. I will follow the notation of [CTDL77] and present only the main results.

A two level system without any perturbation is described by its Hamiltonian  $H_0$ . By using its eigenstates  $|\varphi_0\rangle$  and  $|\varphi_1\rangle$  the stationary Schrödinger

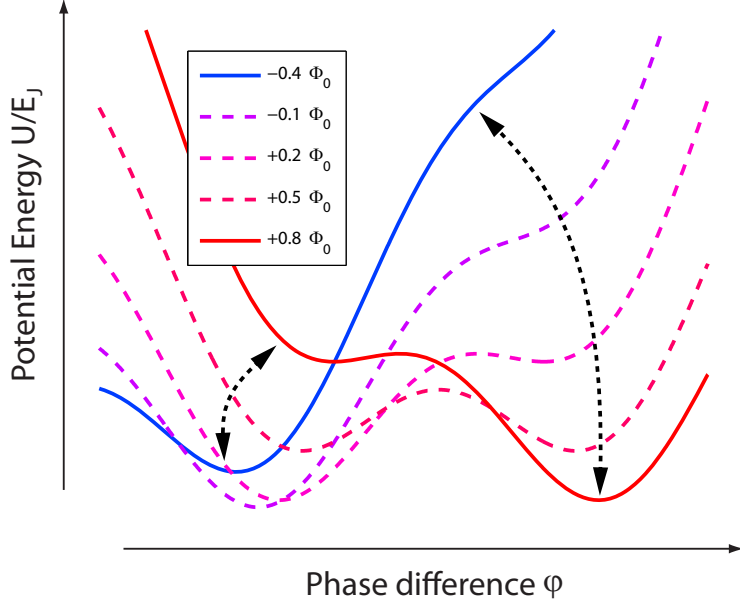


**Figure 2.13:** Potential of the rf-SQUID for different values of applied flux, as denoted in the legend. The red curve shows the potential with the shallow well prepared for qubit operation, while the blue curve shows the deep well at the beginning of initialization. The dashed arrows indicate the tilting of the potential between the beginning and the end of initialization. The corresponding points on the time line are marked in 2.12 with **I** and **II**, respectively.

equation can be written as

$$H_0|\varphi_0\rangle = E_0|\varphi_0\rangle, \quad (2.29)$$

$$H_0|\varphi_1\rangle = E_1|\varphi_1\rangle,$$

where  $E_0$  and  $E_1$  are the corresponding eigenenergies and the Hamiltonian has the diagonal form

$$H_0 = \begin{pmatrix} E_0 & 0 \\ 0 & E_1 \end{pmatrix} \quad (2.30)$$

When we take into account the perturbation, the Hamiltonian reads as

$$H = H_0 + W, \quad (2.31)$$

where  $W$  is the perturbation or coupling operator. For the Hamiltonian  $H$ , we expect both, new eigenenergies  $E_+$  and  $E_-$  and new eigenstates  $|\psi_+\rangle$  and  $|\psi_-\rangle$ . Equation (2.29) then becomes

$$H|\psi_+\rangle = E_+|\psi_+\rangle, \quad (2.32)$$

$$H|\psi_-\rangle = E_-|\psi_-\rangle.$$

The coupling operator is represented by the hermitian matrix

$$W = \begin{pmatrix} W_{00} & W_{01} \\ W_{10} & W_{11} \end{pmatrix} \quad (2.33)$$

where  $W_{00}$  and  $W_{11}$  are real and  $W_{01} = W_{10}^*$ . We assume that  $W_{00} = W_{11} = 0$ , otherwise their effect can be implicitly taken into account by replacing  $E_0$  and  $E_1$  in Eq. (2.30) by  $\tilde{E}_0 = E_0 + W_{00}$  and  $\tilde{E}_1 = E_1 + W_{11}$ , respectively. For the diagonalization of the new Hamiltonian (2.31) we follow the procedure in [CTDL77], which yields the eigenvalues

$$E_{\pm} = \frac{1}{2}(E_0 + E_1) \pm \frac{1}{2}\sqrt{(E_0 - E_1)^2 + 4|W_{01}|^2} \quad (2.34)$$

and the two corresponding eigenvectors

$$|\psi_+\rangle = e^{-i\frac{\varphi}{2}} \cos\left(\frac{\theta}{2}\right) |\varphi_0\rangle + e^{-i\frac{\varphi}{2}} \sin\left(\frac{\theta}{2}\right) |\varphi_1\rangle, \quad (2.35)$$

$$|\psi_-\rangle = -e^{-i\frac{\varphi}{2}} \sin\left(\frac{\theta}{2}\right) |\varphi_0\rangle + e^{-i\frac{\varphi}{2}} \cos\left(\frac{\theta}{2}\right) |\varphi_1\rangle, \quad (2.36)$$

wherein angles  $\theta$  and  $\varphi$  are defined by,

$$\tan \theta = \frac{2|W_{01}|}{E_0 - E_1}, \quad 0 \leq \theta < \pi, \quad (2.37)$$

$$W_{10} = |W_{10}|e^{i\varphi}. \quad (2.38)$$

Since the time evolution of the quantum state is determined by the Schrödinger equation:

$$i\hbar \frac{d}{dt} |\psi(t)\rangle = H |\psi(t)\rangle, \quad (2.39)$$

we can write

$$|\psi(t)\rangle = \lambda e^{-iE_+t/\hbar} |\psi_+\rangle + \mu e^{-iE_-t/\hbar} |\psi_-\rangle, \quad (2.40)$$

wherein  $\lambda$  and  $\mu$  are determined by the initial conditions, for which we define the system to be in the ground state  $|\psi(0)\rangle = |\varphi_0\rangle$  for  $t = 0$ .

Now we can calculate the probability  $P_1(t)$  to find the system in quantum state  $|\varphi_1\rangle$  at a definite time  $t$ . By rewriting Eqs. (2.35) and (2.36) we obtain,

$$|\psi(0)\rangle = |\varphi_0\rangle = e^{i\frac{\varphi}{2}} \left[ \cos\left(\frac{\theta}{2}\right) |\psi_+\rangle - \sin\left(\frac{\theta}{2}\right) |\psi_-\rangle \right]. \quad (2.41)$$

With Eq. (2.40) follows:

$$|\psi(t)\rangle = e^{i\frac{\varphi}{2}} \left[ e^{-iE_+t/\hbar} \cos\left(\frac{\theta}{2}\right) |\psi_+\rangle - e^{-iE_-t/\hbar} \sin\left(\frac{\theta}{2}\right) |\psi_-\rangle \right], \quad (2.42)$$

With this, the probability amplitude, to find the system in state  $|\varphi_1\rangle$  at time  $t$ , is given by

$$\langle \varphi_1 | \psi(t) \rangle = e^{i\frac{\varphi}{2}} \sin\left(\frac{\theta}{2}\right) \cos\left(\frac{\theta}{2}\right) \left[ e^{-iE_+t/\hbar} - e^{-iE_-t/\hbar} \right]. \quad (2.43)$$

For the probability  $P_1(t) = |\langle \varphi_1 | \psi(t) \rangle|^2$  we then obtain

$$\begin{aligned} P_1(t) &= \frac{1}{2} \sin^2 \theta \left[ 1 - \cos \left( \frac{E_+ - E_-}{\hbar} t \right) \right] \\ &= \sin^2 \theta \sin^2 \left( \frac{E_+ - E_-}{2\hbar} t \right), \end{aligned} \quad (2.44)$$

which after consideration of (2.34) and (2.37) reads as

$$P_1(t) = \frac{4|W_{01}|^2}{4|W_{01}|^2 + (E_0 - E_1)^2} \sin^2 \left[ \frac{t}{2\hbar} \sqrt{4|W_{01}|^2 + (E_0 - E_1)^2} \right]. \quad (2.45)$$

Known as Rabi's formula, Eq. (2.45) describes a sinusoidal oscillation of  $P_1$  at the Rabi frequency

$$\omega_R = \frac{1}{2\hbar} \sqrt{4|W_{01}|^2 + (E_0 - E_1)^2}, \quad (2.46)$$

and with an amplitude

$$A_R = \frac{2|W_{01}|^2}{4|W_{01}|^2 + (E_0 - E_1)^2}. \quad (2.47)$$

$2A_R$  is close to one if the coupling is strong, or  $|W_{01}| \gg |E_0 - E_1|$ .

A further discussion, including decoherence effects and detuning the microwave frequency from the transition frequency and the consequences for Rabi frequency and amplitude, can be found in [Lis03].

The off-diagonal (coupling) matrix element of the Hamiltonian can be reduced to be proportional to the microwave amplitude by applying the rotating wave approximation and is then given by [MNA<sup>+</sup>03]

$$|W_{01}| = \langle 0 | \varphi | 1 \rangle \frac{\Phi_0}{2\pi} I_{\text{rf}}, \quad (2.48)$$

where  $I_{\text{rf}}$  is the absolute amplitude of the alternating current. If we assume the potential is sufficiently harmonic for  $U(\varphi) \lesssim E_1$ , we can look up the result for the harmonic oscillator to find

$$\langle 0|\varphi|1\rangle = \sqrt{\frac{\hbar}{2m\omega_{01}}} = \frac{2\pi}{\Phi_0} \sqrt{\frac{\hbar}{2\omega_{01}C_j}}, \quad (2.49)$$

where the effective mass of the virtual particle  $m = C_j(\Phi_0/2\pi)^2$  has been inserted. For the case of strong coupling ( $|W_{01}| \gg |E_0 - E_1|$ ), we find the Rabi frequency from Eq. (2.46), which reduces to

$$\omega_R = \frac{|W_{01}|}{\hbar}, \quad (2.50)$$

Finally, we obtain

$$\omega_R = \frac{I_{\text{rf}}}{\hbar} \sqrt{\frac{\hbar}{2\omega_{01}C_j}} = I_{\text{rf}} \sqrt{\frac{1}{2\hbar\omega_{01}C_j}}. \quad (2.51)$$

## Chapter 3

# Dispersive readout scheme of the SQUID resonator

For the flux qubit [MOL<sup>+</sup>99], non-destructive dispersive readout schemes were implemented in the past by coupling either to a high-quality LC-resonator circuit [IOI<sup>+</sup>03] or to a dc-SQUID [LmcVS<sup>+</sup>04].

So far, most measurements of phase qubits have been performed typically by the switching current measurement of an inductively coupled dc-SQUID. Recently, an experiment overcoming the limitations of the switching readout was reported [SKD<sup>+</sup>10]. In this approach, the phase qubit was capacitively coupled to a transmission line which allows for direct probing of its resonance frequency with a microwave pulse. This approach eliminates a readout dc-SQUID, but introduces decoherence via the line coupled directly to the qubit.

This chapter is dedicated to the new microwave readout system, going to be applied to the phase qubit, which has been described before in section 2.3. There the readout was based on the conventional technique, the switching current measurement of a dc-SQUID which is inductively coupled to the qubit. For each readout event the switching of the SQUID to the non superconducting state generates heat directly on the chip and quasi-particles in the circuitry. Both effects are responsible for a relatively long cool-down time of about 1-2 ms required after each switching event. Together with the time needed to ramp up the bias current of the SQUID, this limits the repetition rate of the experiment.

As it has been described in section 2.1, a Josephson junction itself already forms an LC-resonator. The resonance frequency

$$f = \frac{1}{2\pi\sqrt{L_J C_J}}, \quad (3.1)$$

is determined by the Josephson inductance given by Eq. (2.8) and the capacitance

$$C_J = \frac{\varepsilon_0 \varepsilon_r A}{d}, \quad (3.2)$$

where  $\varepsilon_r$  is the dielectric constant of the material forming the oxide layer and  $d$  is the thickness of this layer separating the two superconducting electrodes, each of the area  $A$ .

By combining the Josephson inductance of a single junction, given by Eq. (2.8) and the first Josephson Eq. (2.3) written in the form  $\varphi = \arcsin(I_b/I_c)$ , we obtain the Josephson inductance in dependence of the junction critical current  $I_c$  and the bias current  $I_b$ :

$$L_J(I_c, I_b) = \frac{\Phi_0}{2\pi} \frac{1}{I_c \cos(\arcsin(I_b/I_c))} = \frac{\Phi_0}{2\pi} \frac{1}{\sqrt{I_c^2 - I_b^2}}. \quad (3.3)$$

### 3.1 SQUID-resonator in the linear regime

A dc-SQUID can be considered in its behavior similar to a single Josephson junction with a critical current  $I_c(\Phi)$  which is tunable by an externally applied magnetic flux  $\Phi$ . By introducing the flux dependent critical current  $I_{c,\text{SQUID}}(\Phi)$  of the dc-SQUID given by Eq. (2.27), we obtain the Josephson inductance of the dc-SQUID

$$L_J(\Phi, I_b) = \frac{\Phi_0}{2\pi} \frac{1}{\sqrt{\left(2I_{c0} \left|\cos\left(\frac{\pi\Phi}{\Phi_0}\right)\right|\right)^2 - I_b^2}} \quad (3.4)$$

where  $I_{c0}$  is the critical current of a single junction in the SQUID. For a SQUID bias current  $I_b = 0$  this reduces to

$$L_J(\Phi) = \frac{\Phi_0}{4\pi I_{c0} \left| \cos\left(\frac{\pi\Phi}{\Phi_0}\right) \right|} \quad (3.5)$$

For a critical current of a single junction  $I_{c0} = 2 \mu\text{A}$  the dependence of the Josephson inductance of the SQUID on the applied flux is shown in Fig. 3.1.

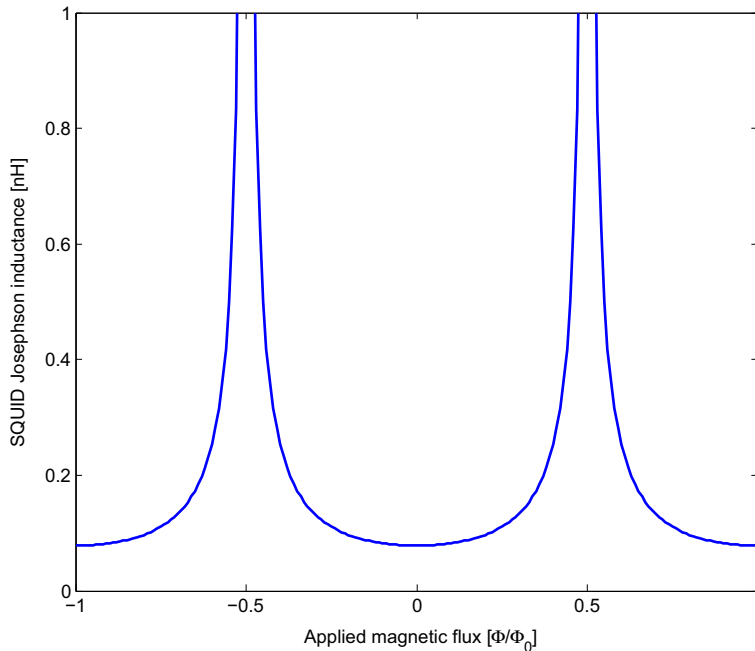


**Figure 3.1:** Dependence of the Josephson inductance of the SQUID on the applied magnetic flux as given by Eq. (3.5). The critical current of a single junction of the SQUID is  $I_{c0} = 2.1 \mu\text{A}$ , giving a minimal Josephson inductance  $L_{J0} = 78.4 \text{ pH}$ .

For typical values  $L_J = 160 \text{ pH}$  and  $C_J = 320 \text{ fF}$  of a single Josephson junction in our samples this yields a resonance frequency in the range of  $f \approx 22 \text{ GHz}$ . This high frequency is somewhat inconvenient to use, since it is in the frequency range of the energy level splitting of the qubit. An additional more practical reason to prefer working at lower frequencies is,

that these frequencies are easier accessible with our standard lab equipment, eg. microwave sources, power splitters, mixers which usually have an upper frequency limit of 20 GHz. The reduction of the resonance frequency of the SQUID resonator is therefore achieved by an additional shunt capacitor  $C_1$  which is shown in the schematic of the resonator circuit in Fig. 3.2. The probe signal is applied via a coupling capacitor  $C_0$  which serves as high pass filter to protect the SQUID from low frequency noise and to avoid any dc-current flow through the SQUID.

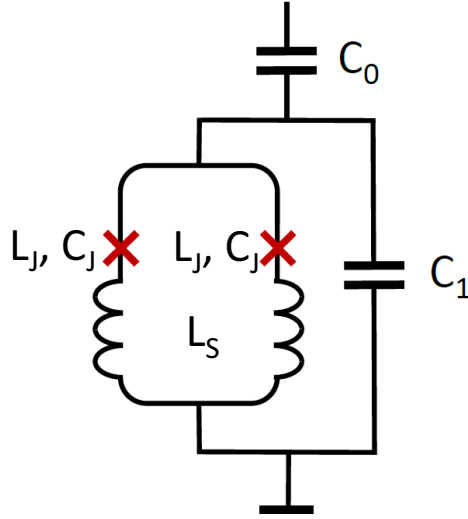


**Figure 3.2:** Schematic of the SQUID-resonator circuit. Josephson junctions are indicated by red crosses with their Josephson inductance  $L_J$  and their capacitance  $C_J$  respectively.  $L_S$  denotes the SQUID loop inductance, and  $C_1$  the capacitance of the shunt capacitor. The probe signal is applied via the coupling capacitor  $C_0$ .

The shunt capacitor  $C_1$ , the SQUID loop inductance  $L_S$  and Josephson inductance  $L_J$  form a lumped element resonator with a resonance frequency given by

$$f_{\text{res}} = \frac{1}{2\pi\sqrt{(L_S + L_J)C_1}} \quad (3.6)$$

where the capacitances  $C_J$  of both junctions are already included in  $C_1$ , since

they are two orders of magnitude smaller than  $C_1$ .

With the flux dependent Josephson inductance, as written in Eq. (3.5), the flux dependent resonance frequency is then given by

$$f_{\text{res}}(\Phi) = \frac{1}{2\pi \sqrt{\left( L_S + \frac{\Phi_0}{4\pi I_{c0} \left| \cos\left(\frac{\pi\Phi}{\Phi_0}\right) \right|} \right) C_1}} \quad (3.7)$$

The expected dependence of the resonance frequency on the externally applied flux, for sample parameters yielding a maximum resonance frequency  $f = 1.93$  GHz, is shown in Fig. 3.3.

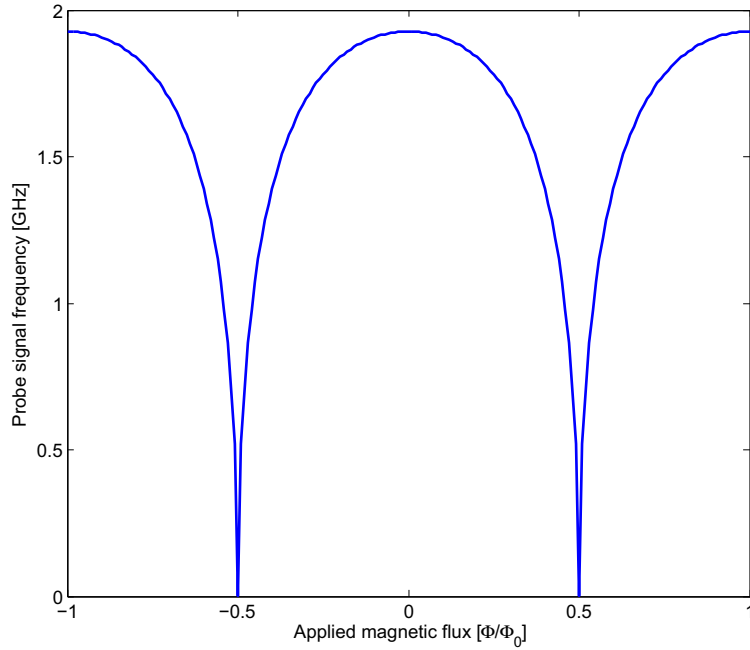


**Figure 3.3:** Dependence of the resonance frequency of the SQUID-resonator on the applied magnetic flux as given by Eq. (3.7).

In this section we considered the driving power of the microwave signal, probing the resonator to be low, corresponding to a small AC current in the SQUID compared to its critical current. This leads to a behavior of the

system according to a linear oscillator which does not show a dependence of the resonance frequency on the driving power. This low power, linear regime is later going to be used for the readout of the qubit which will be described in section 4.4

### 3.2 SQUID-resonator in the non-linear regime

For a higher driving power the non-linearity of the SQUID introduces qualitatively new features which can be seen in the measurement data shown in Fig. 3.4. The figure shows the amplitude of the microwave signal reflected from the SQUID-resonator versus the applied frequency.

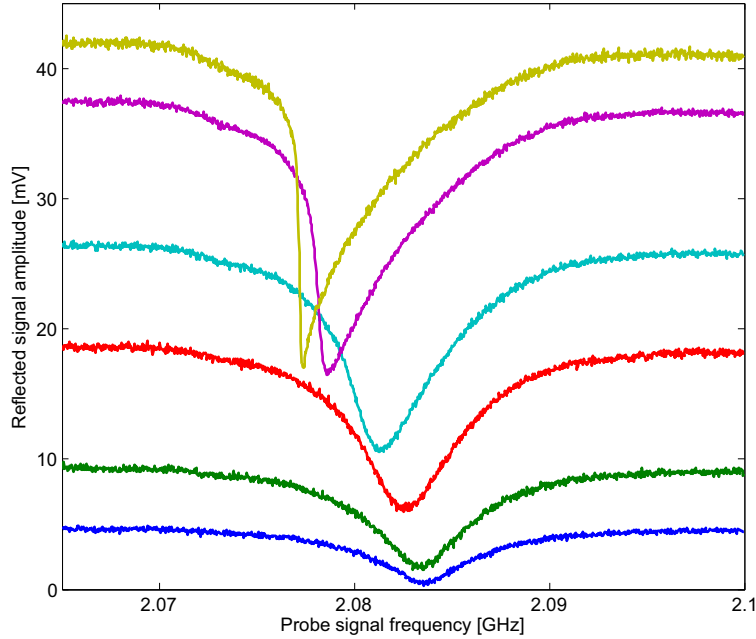


**Figure 3.4:** Resonance curves of the SQUID-resonator for different values of the microwave drive power. From bottom to top: -18dBm, -12dBm, -6dBm, -3dBm, 0dBm and 3dBm respectively at the output of the network analyzer. See text for a more detailed description.

The measurement was performed by a vector-network-analyzer and is usually referred to as  $S_{11}$  measurement. Each curve corresponds to a different

microwave drive power according to the values shown in the figure caption. The power is increased from the bottom to the top curve. Each curve shows a dip in the spectrum at the resonance frequency, typical for a reflection measurement on a resonator.

For low driving powers the curves show a symmetric Lorentzian shape as expected for a linear oscillator. As the driving power is increased the resonance curves become asymmetric and the maximum shifts to lower frequencies. This behavior is described by the dynamics of the Duffing oscillator, a driven oscillator with a restoring force asymmetric around the origin. A more detailed discussion of the Duffing oscillator in general can be found in [Bla66], while a further investigation of the non-linear regime of the SQUID resonator and its application for reading out a flux qubit can be found in [Lup05].

While already in the non-linear regime of the resonator, an even stronger driving at higher microwave power results in a bistable behavior of the system with hysteresis [SVP<sup>+</sup>04], [VDS09]. By using this bifurcation regime, a quantum non-demolition readout of a flux qubit has already been realized [LSP<sup>+</sup>07].

For the readout of a phase qubit on the other hand, the qubit states are mapped to distinct flux states, which differ on the order of one  $\Phi_0$  in the qubit loop. Therefore the sensitivity of the SQUID in the linear regime is already high enough to perform a single shot readout of the phase qubit. In this thesis only the linear regime is used for the readout of the phase qubit and will be referred to in chapter 5.3.

While the operation of the readout in the linear regime and in the nonlinear regime below the bifurcation point serves very well in a destructive readout scheme for the phase qubit, the extremely sensitive bifurcation readout regime mentioned above may give rise to the possibility of a direct quantum non-demolition readout of a phase qubit.



# Chapter 4

## Experimental Technique

In this chapter, the measurement techniques used to obtain the data presented in Chapter 5 are described. We are starting with a description of the samples that have been measured and continue to report about the different types of measurement setups that have been used.

The low temperature laser scanning microscopy (LTLSM) setup which was used to characterize the resonator structures is described in section 4.2. The main part of chapter 4 is attributed to the description of the two different types of electronic setups that have been used for the switching current readout of the qubit (section 4.3) on one hand and for the dispersive readout of the qubit (section 4.4) on the other hand.

### 4.1 Sample design and fabrication

The measured samples were fabricated by a commercial foundry on 5 x 5 mm<sup>2</sup> oxidized Silicon chips by using superconductive integrated circuit technology, including photolithography. Silicon-oxide (SiO<sub>2</sub>) is used as an insulator between the superconducting layers. Figure 4.1 shows an optical micrograph of the measured structure.

While the design was done for a  $J_c = 30$  A/cm<sup>2</sup> process, the fabrication yielded a critical current density of  $J_c = 27$  A/cm<sup>2</sup>. Together with the designed junction diameter of 3  $\mu$ m this leads to critical current  $I_c = 1.91$   $\mu$ A of both, the qubit junction as well as the SQUID junctions. This in turn gives,

according to Eq. (2.8) a minimum Josephson inductance  $L_{J0} = 172$  pH for a single junction, and  $L_{J0,SQUID} = 86$  pH for the SQUID. The SQUID loop has a size of  $78.5 \times 75.5 \mu\text{m}^2$ , so the loop inductance is calculated with FastHenry [Whi] to  $L_S = 111$  pH. For symmetry reasons the SQUID shunt capacitor  $C_1 = 36.6$  pF is combined from two capacitors in parallel with a designed capacitance of  $C_1/2 = 18.3$  pF and a size of  $97 \times 97 \mu\text{m}^2$  each. The inductance of the SQUID loop  $L_S = 111$  pH, the minimum Josephson inductance of the SQUID  $L_{J0,SQUID} = 86$  pH and the capacitance of the shunt capacitor  $C_1 = 36.6$  pF yield, according to Eq. (3.6) a resonance frequency of the structure  $f = 1.87\text{GHz}$ . The qubit loop inductance was calculated ([Whi]) to  $L_{\text{qubit}} = 644$  pH, which gives, according to Eq. (2.24),  $\beta_L = 4.1$ . The coupling between the qubit and the SQUID is defined by the mutual inductance of the two loops  $M = 30$  pH.

## 4.2 LTLISM setup

For the first characterization of our resonator structures we used the technique of low temperature laser scanning microscopy (LTLISM). The sample is mounted on a copper table which is cooled by volume of approximately 1 liter of  $^4\text{He}$ . The top cover of the cryostat is fitted with an optical window which allows the laser beam from the room temperature optical setup to enter. The illuminated spot is scanned over the surface of the sample and allows for different modes of imaging. Figure 4.2 shows a photograph of the LTLISM setup with the cryostat containing the sample and the optical system on top.

Figure 4.3 shows a schematic drawing of our custom made [Luka] stainless steel LTLISM cryostat, with a cross-sectional view on the left and a top view on the right. An inside view of this cryostat is shown in Fig. 4.4.

The LTLISM can be operated in several different modes [ZST<sup>+</sup>06], depending on the properties of the sample that should be determined by the measurement. Here I will only refer to the two modes that were used to obtain the measurement results shown in this thesis in section 5.1.

The reflectivity measurement is done to obtain the optical properties of the sample. For this, a modulated, sharply focused laser beam is used as a

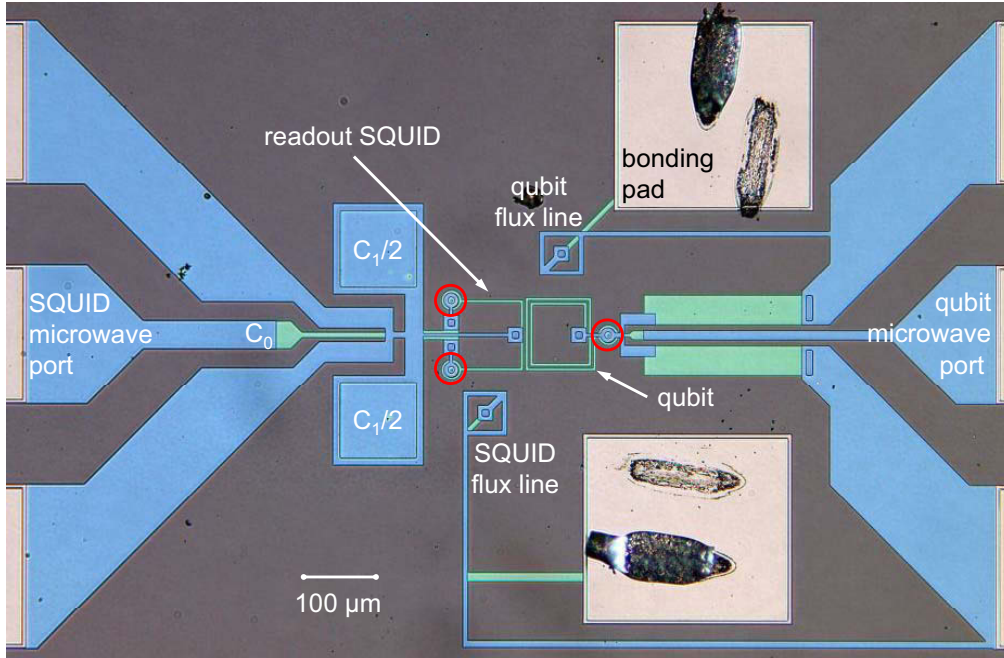


**Figure 4.1:** Optical microscope image of the measured structure. Different colors correspond to different layers of metallization: blue: top layer; green: bottom layer; light grey: contact pads; dark grey: substrate. Josephson junctions are indicated by red circles. The SQUID loop with the shunt capacitors  $C_{1/2}$  and the coplanar microwave launcher is shown on the left, with its flux line below.  $C_0$  is a coupling capacitor which serves for protecting the SQUID from dc and low frequency noise. The qubit and its microwave port are located on the right side, with the corresponding flux line above. A detailed description of the layout is given in the text.

probe, scanned over the surface of the sample. The reflected laser power is detected by a photo diode as a function of the probe coordinates  $x$  and  $y$ . The output of the photo diode is amplified using lock-in technique, synchronized to the laser modulation. A data acquisition card in the measurement computer is used to digitize the signal. This so called optical contrast mode is used

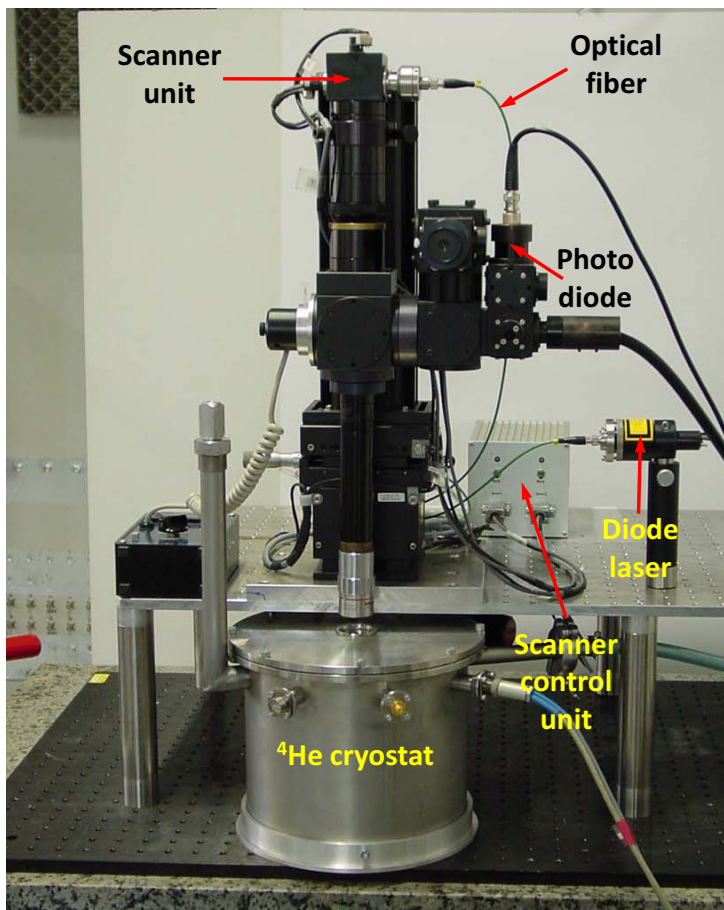


**Figure 4.2:** LTLSM setup showing the cryostat containing the sample and the optical system on top. A diode laser (right) generates the probe signal which is fed into the scanner unit at the top of the optical system by an optical fibre. Two mirrors, one for the x and y direction each, allow for a deflection of the laser beam which is controlled by software on the measurement computer via the scanner control electronics. A photo diode allows for measurement of the reflected laser power.

here to establish a correlation to the microwave photo response mode, the second operation mode of the LTLSM that we used in further measurements.

The absorbed part of the laser energy heats the sample locally for probing the thermosensitive microwave transmittance  $S_{21}(f)$  of the sample. The

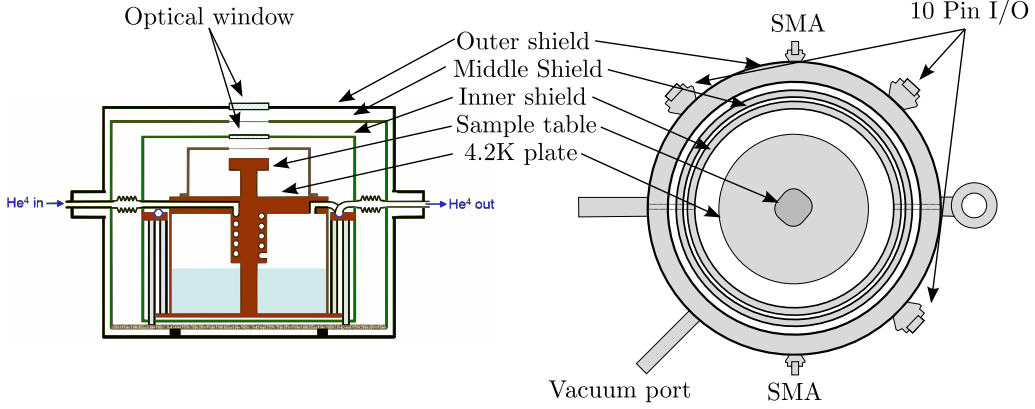


**Figure 4.3:** Schematic drawing of the LTLSM cryostat [Luka], cross-sectional view on the left side and top view on the right side. The sample is mounted on the sample table in middle (brown) and is cooled by the Helium bath underneath. Several radiation shields (green) protect the sample and bath from room temperature heat radiation, while windows on top allow for optical access.

thermally induced changes of  $S_{21}(f)$  by the probe are understood as microwave photo response (PR) and can be expressed as

$$PR \propto \frac{\partial |(S_{21}(f))|^2}{\partial T} \delta T \quad (4.1)$$

It has been shown in [CNW98] that the modulation of the kinetic inductance by the thermal probe allows one to measure a quantity proportional to

$$A \lambda_{\text{eff}}^2(x, y) J_{\mu w}^2(x, y) \delta \lambda_{\text{eff}}, \quad (4.2)$$

where  $A$  is illuminated area,  $\lambda_{\text{eff}}$  is the local magnetic penetration depth,  $J_{\mu w}$  is microwave current density and  $\delta \lambda_{\text{eff}}$  is the light-induced change in  $\lambda_{\text{eff}}$ . This consequently can be used to extract  $J_{\mu w}^2(x, y)$  maps.

In the microwave photo response mode the sample is supplied with a microwave signal generated by a commercially available source which is controlled by the measurement computer via GPIB. Together with an appropriate diode or a spectrum analyzer serving as a detector this setup allows

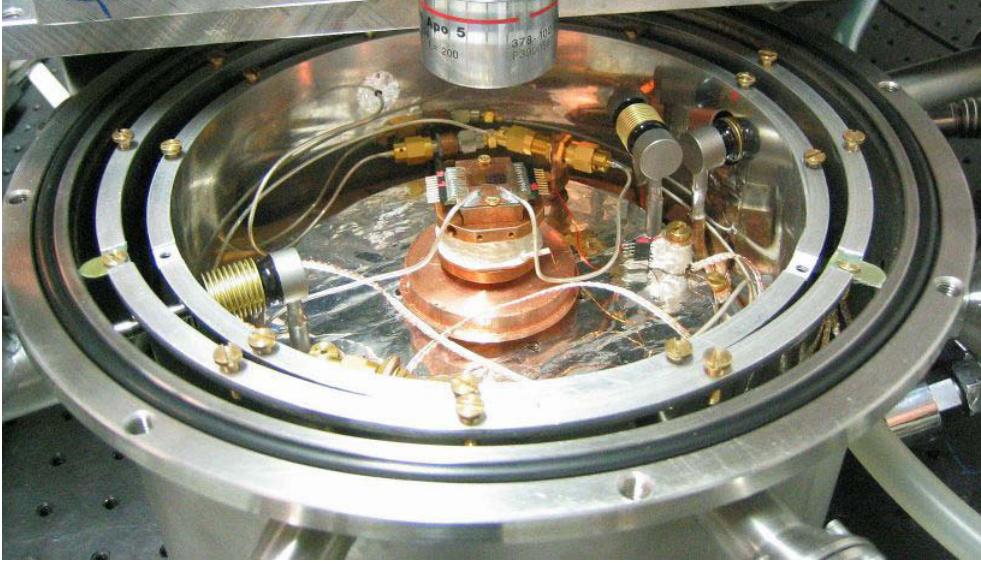


**Figure 4.4:** LTLSM cryostat without top cover. The 5 mm  $\times$  5 mm sample chip is located in the middle on the sample holder underneath the objective lens of the microscope. The sample holder is attached to the copper table which is in thermal contact to the Helium volume underneath. Everything is contained in a stainless steel vessel which is evacuated for operation. Two concentric radiation shields made from aluminium protect the sample and the Helium volume from the room temperature radiation.

for measurements of the microwave transmittance  $S_{21}(f)$  of the sample, as it is done in [ZST<sup>+</sup>06]. Our measurement is carried out in a little different way, since we are measuring the microwave reflectance  $S_{11}(f)$  of the SQUID resonator. Since the microwave transmittance  $S_{21}(f)$  and the microwave reflectance  $S_{11}(f)$  of a dissipationless device are linked by

$$|(S_{11}(f))|^2 + |(S_{21}(f))|^2 = 1, \quad (4.3)$$

and therefore

$$\delta|(S_{11}(f))|^2 = -\delta|(S_{21}(f))|^2, \quad (4.4)$$

what was said above can also be applied to the detection of the thermally induced change of  $S_{11}(f)$ , the microwave signal reflected from the SQUID resonator.

Figure 4.5 illustrates the method of extraction of the data. Two resonance curves are plotted in Fig 4.5(a), how they would be obtained by a reflection measurement with a vector network analyzer. The blue curve corresponds to the  $|S_{11}|^2$  characteristics for the unperturbed resonator, while the red curve corresponds to the  $|S_{11}|^2$  characteristics of the resonator perturbed by the laser. Figure 4.5(b) shows the difference of the two traces in (a), corresponding to the shift of the microwave reflectance  $\partial|(S_{11}(f))|^2$  of the resonator by the LSM probe.

It has been shown in [ZST<sup>+</sup>06] that the total LSM microwave photoreponse  $\partial|(S_{12}(f))|^2$ , and therefore according to Eq. (4.4) also  $\partial|(S_{11}(f))|^2$  has contributions from the effect of the resonance frequency detuning  $\delta f_0$  and the broadening  $\Delta f_{3\text{dB}}$  of the resonance curve. The resonance frequency detuning is associated with the change of the kinetic inductance due to the thermal probe, while the broadening is directly related to the light-induced modulation of the inverse quality factor due to an increase in local Ohmic dissipation. At temperatures well below  $T_C$  the microwave current driven resistive component of the photo response can be neglected, and only the inductive component produces contrast [ZUHA02, CNW98] in the LSM photo response, due to modulation of the kinetic inductance of the resonator by the thermal probe. This allows to measure a quantity proportional to  $J_{\mu\text{w}}^2(x, y)$ . [NC93] The according measurement on the resonators are shown in section 5.1.

Figure 4.6 shows a schematic of one of the microwave setups that were used for the measurements. The band of the circulator, from 1.7 GHz to 2.4 GHz puts the limitation of usage to this frequency range. The signal level of the source can be reduced by a step attenuator before it passed through the circulator to the sample. A dc-break serves for protecting the sample from low frequency noise, while the 10 dB attenuator is used for impedance matching, to reduce reflections due to mismatches at the transition from the cable to the sample holder and further to the chip. The reflected signal passes the circulator again and is then amplified by two amplifiers in series to achieve a signal level that is high enough to operate the detector diode

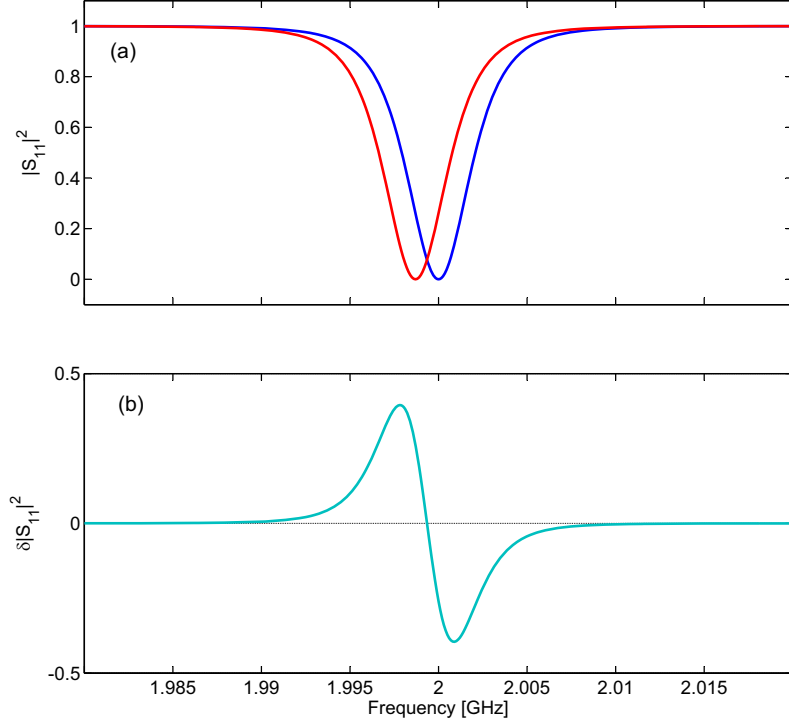


**Figure 4.5:** (a) Microwave reflectance of a resonator for 'laser off'(blue), and 'laser on'(red). (b) Difference of the two traces in (a), that is proportional to the LSM microwave photo response according to Eq. (4.1)

at its working point. The isolator between the two amplifiers avoids signal reflections from the input port of the second amplifier which could excite the first amplifier and lead to oscillations between the two amplifiers, driving them into saturation.

Figure 4.7 shows the schematic of the setup modified for a broader frequency range from 1.5 GHz to 4 GHz. The narrow band circulator as the limiting element has been replaced by a directional coupler with a larger bandwidth. A second directional coupler is used here, directly at the output of the microwave source for a different reason. By applying a microwave current larger than the critical current of the Josephson junctions in the

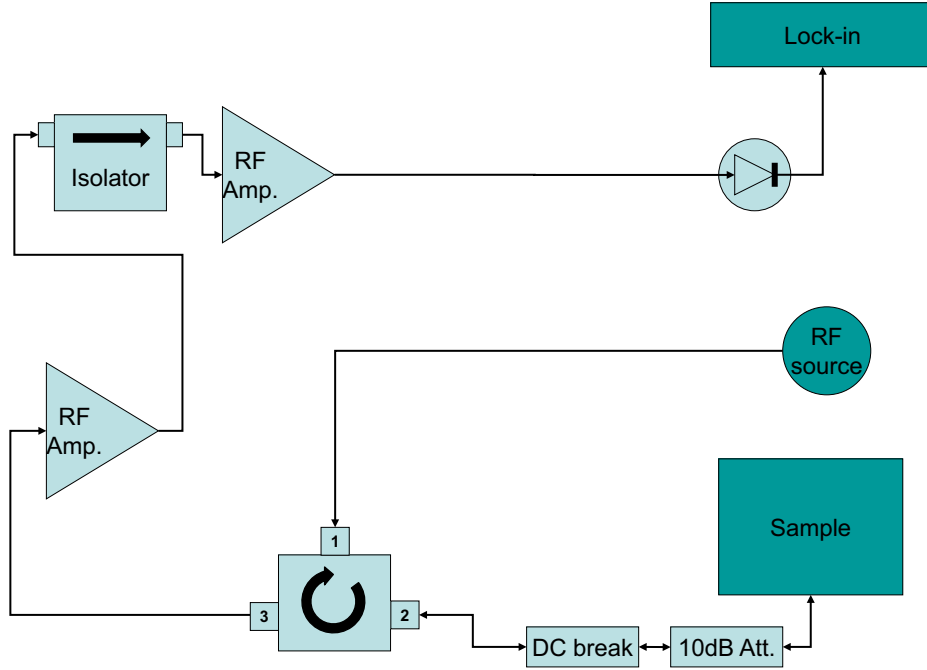


**Figure 4.6:** Schematic of the LTLSM microwave setup for measurements in the frequency range from 1.7 GHz to 2.4 GHz, limited by the bandwidth of the circulator.

SQUID one would bring them to the resistive state and microwave power would be dissipated. To avoid this one should operate at low microwave powers applied to the SQUID. As the power should be large enough operate the detector diode at its working point, the second directional coupler is used as a power splitter, allowing the signal from the source to be directly used as bias for the detector diode. The other branch, which carries the signal propagating to the sample, is coupled to the source with an attenuation of 20 dB. An additional step attenuator is used to adjust the signal level at the sample independently from the output power of the source. The reflected signal is amplified as mentioned for the setup before and is then combined with the bias signal just before the detector diode.

The measurements of the optical contrast and the microwave photo

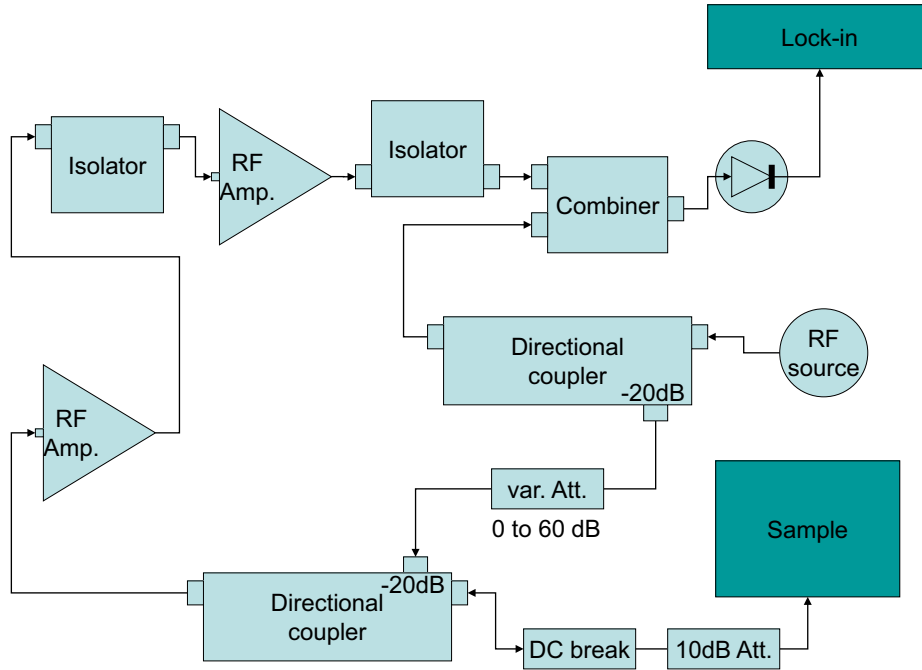


**Figure 4.7:** Schematic of the LTLSM microwave setup for measurements in a wider frequency range from 1.5 GHz to 4 GHz. The circulator as the bandwidth limiting element has been replaced by a broad band directional coupler. See text for detailed description.

response which were done in the different operation modes of the LTLSM described here, are shown in section 5.1.

### 4.3 Switching current measurement setup

This work mainly concentrates on the dispersive readout of a Josephson phase qubit by probing the detector SQUID with a weak microwave tone.

To be able to compare this new type of readout with the conventional readout of Josephson phase qubits that has been used so far, comparative measurements have been done. The samples for both measurements have been produced during the same fabrication run to make them comparable

with respect to the junction parameters and to avoid changes between two runs in the inevitable deviation of the designed parameters from the actually fabricated ones.

The conventional readout of a Josephson phase qubit relies on the recording of the switching current of the dc-SQUID which is determined by the flux state of the qubit that is inductively coupled to the SQUID.

In the following section we therefore describe the electronic setup that has been used to perform the switching current measurements.

#### 4.3.1 Wiring and filtering

The sample is placed inside a closed copper cell, see Figures 4.8 and 4.9, thermally anchored to the mixing chamber of an Oxford  $^3\text{He} / ^4\text{He}$  dilution refrigerator, which has a base temperature of about 20 mK. Wires are connected to the readout-SQUID for current-biasing and measuring the voltage drop across it.

The leads pass through a series of filters and current dividers to shield the qubits from noise. Custom-made microwave filters [WLC<sup>+</sup>03] are installed close to the sample housing. These consist of a long resistive wire furled inside a copper tube which is filled with a mixture of STYCAST<sup>TM</sup> 2850 FT [Eme] and copper powder. Each grain is isolated from another by a naturally grown oxide layer. Due to the large net surface of the powder, skin-effect losses are substantial and this kind of filter provides an attenuation of more than 50 dB above 1 GHz. On top of the sample holder every wire passes through a  $\pi$ -type feedthrough filter [Spe]. The next filter stage consists of RC low pass filters with a cutoff frequency of around 50 kHz, thermally anchored to the 1 K pot of the cryostat. At room temperature, the leads finally pass through another stage of  $\pi$ -type feedthrough filters with a cutoff of about 10 MHz before they are connected to the analog electronics.

Inside the copper cell, the flux line as well as microwave line of the qubit are connected to coaxial cables. These semi-rigid cables are made from copper up to the 1 K pot. Each microwave cable has a 10 dB attenuator [Aer] thermally anchored to the mixing chamber and another 10 dB attenuator thermally anchored to the 1 K pot. From there towards the top of the

cryostat, semi-rigid cables made from stainless steel are used to provide a good thermal isolation. At room temperature, a bias-tee on the flux line allows for feeding the bias current together with the nanosecond long flux-pulses.

### 4.3.2 Electronics

In the following section, the electronics are described. By function, the electronics can be divided in two main parts. One part is used for the current ramp measurement to determine the switching current of the dc-SQUID. The second part controls the flux line currents and generates the flux pulse sequences. Figure 4.10 shows a block diagram of the switching current measurement setup.

#### Qubit control

The qubit is controlled by the external flux bias to tilt the rf-SQUID potential to the working point, as described in section 2.3.1. A microwave pulse is applied to populate the first excited state of the two level system. Finally a flux pulse is applied to allow tunneling from the first excited state.

**The qubit flux bias** is provided by two current sources, which are controllable independently. The output current is proportional to a control voltage by a factor of  $10^{-3}\text{A/V}$  for the first, and by a factor of  $10^{-4}\text{A/V}$  for the second source. The current outputs are added and connected via a coaxial line and an attenuator (see section 4.3.1) to the flux bias loop. The control voltages are generated by DACs inside the shielded room. The DACs are controlled by a DAC logic, which is connected to the output of a NIDAQ card outside the shielded room via an optical fiber link. The DAC outputs are not directly connected to the input of the corresponding current source, but via a multiplexer, a switch, controlled by a gate signal. When a signal is applied to the start gate of the multiplexer, the output is connected to input  $U_1$ . Without a gate signal, the output is connected to input  $U_0$ . This allows to switch the input of the current source between two fixed voltages. The

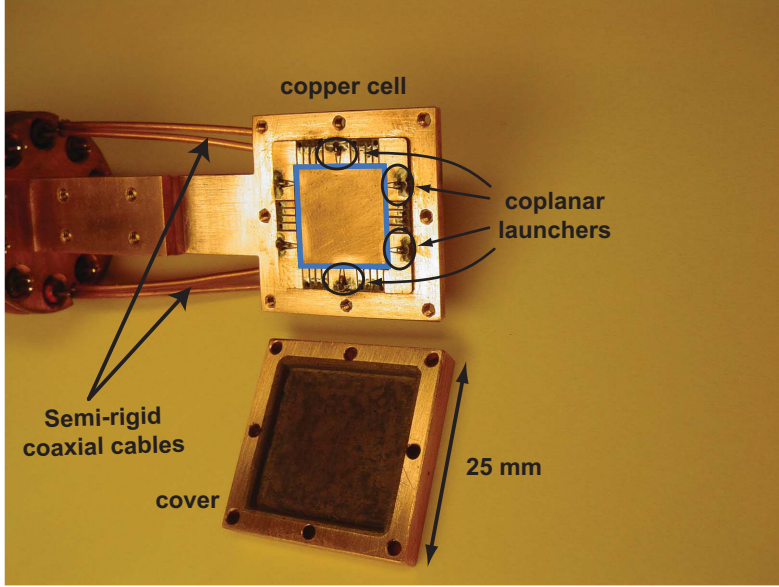


**Figure 4.8:** Sample holder [Lukb] with opened copper cell. Semi-rigid coaxial cables coming from the left side, enter the copper cell from the back and are soldered to coplanar launchers. The blue square denotes the area of  $15 \times 15 \text{ mm}^2$ , to where the samples can be glued. The inner side of the cover is coated with a 1 mm thick mixture of STYCAST<sup>TM</sup> epoxy and copper powder to reduce the amplitude of standing waves in the sample cell.

first multiplexer (MPX1) switches the output of DAC1 or DAC3 to the input of the first current source, thus changing the flux bias from the beginning of the initialization sequence (marked by **I** in Fig. 2.12(a)) to  $\Phi \approx \Phi_0$ . The second multiplexer (MPX2) switches the output of DAC2 or zero voltage to the input of the second current source, thus allowing to switch the additional small field on and off.

To map the phase states of the two level system to flux states of the rf-SQUID, a flux pulse is applied, which allows immediate tunneling from the first excited state. This flux pulse is typically 1 ns long and is generated by an Agilent 81130A pulse generator. The generator is located outside the shielded room and is connected via 10 dB attenuator to a SMA feed-through connector, which is installed on the wall of the shielded room. On top of the

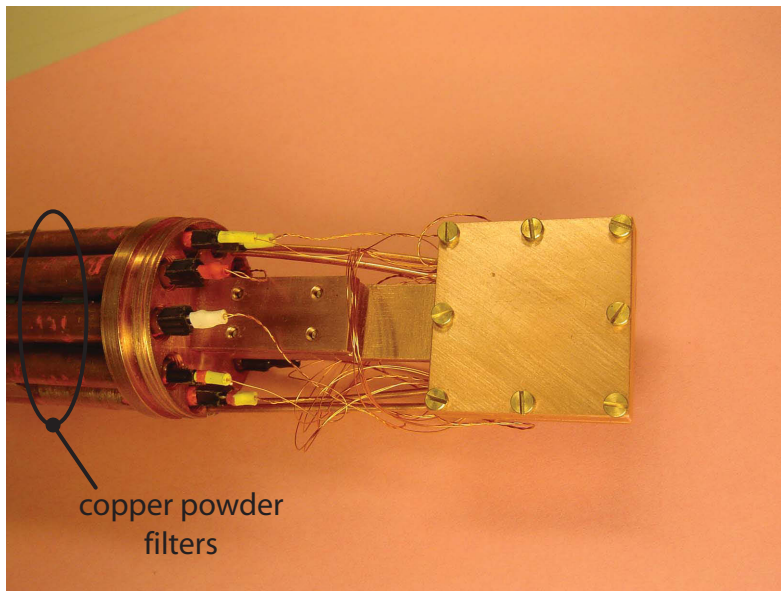


**Figure 4.9:** Sample holder with closed cover of the copper cell. The twisted pair wires leave the copper cell at the back side and are connected to the copper powder filters, which can be seen on the left side of the picture.

cryostat a bias-tee combines the flux pulse and the dc flux bias currents.

**The qubit rf-bias** is generated by a microwave generator. The microwave pulse is shaped by mixing it with a DC-pulse, generated by the Agilent E81130 pulse generator. Two mixers are connected in series to the output of the rf-source to increase isolation. Before the signal enters the shielded room, it is attenuated by 20 dB to reduce noise in the microwave line. The intermediate frequency inputs of the mixers are connected to the output of the pulse generator via a power divider. Several attenuators and low pass filters provide a pulse of appropriate shape and amplitude. These characteristics are checked with a 1 GHz oscilloscope.

### 4.3. Switching current measurement setup

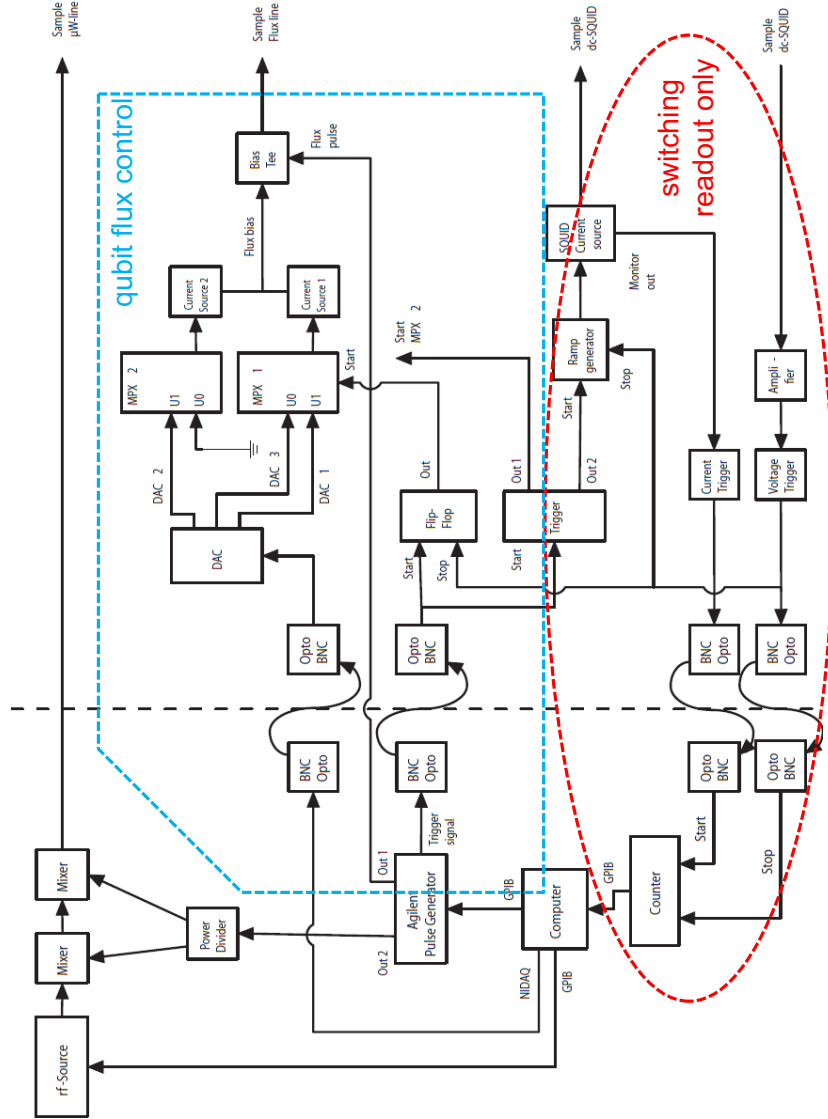


**Figure 4.10:** Electronic setup for qubit control and switching readout. Electronics, necessary only for the switching readout is indicated by the red dashed line. Qubit flux control electronics, also used with the new readout is indicated by the blue dashed line. Rotate clockwise for better view. Filters and attenuators are not shown for a better overview. Devices on the left side of the black dashed line are located in a rack outside the shielded room. The other electronics is installed inside the shielded room. The explanation of the setup is given in the text.

### Qubit readout

Together with the cryostat, and the electronics mentioned above to control the fluxes, the electronics to control the dc-SQUID is installed in the shielded room. A sawtooth generator with adjustable ramp rate and trigger inputs (to start and stop the ramp) drives the current source, biasing the readout-SQUID. The current is ramped up and a trigger signal is delivered when the current crosses zero. The voltage across the junction is monitored and as soon as a voltage drop across the junction is registered, a second trigger signal is generated, which switches off the current ramp immediately. Both trigger signals are guided outside the shielded room via optical fibers to guarantee electrical isolation between the biasing electronics and data acquisition devices. A time interval counter with a time-base of 20 GHz is used to measure the time  $\Delta t$  between the pulses indicating the zero-crossing of the bias and the switching of the dc-SQUID.

With the knowledge of the ramp rate  $dI/dt$ , the switching current is reconstructed via  $I_{sw} = dI/dt \Delta t$ . The experiment is typically repeated 500 times per second, stimulated by the Agilent 81130A pulse generator connected to the start gate of the multiplexers to provide the flux pulses and the ramp generator via an additional optical fiber. A further and more detailed description of the current ramp measurement can be found in [Lis03].

Data acquisition is done by a computer connected to the counter via a GPIB interface. Custom-made software based on MATLAB<sup>TM</sup> allows for on-line calculation of the switching current distribution and the escape probability, and provides the means to control any further device like flux line current sources, microwave generators and temperature control.

## 4.4 Measurement setup for dispersive readout

In this section we are going to describe the measurement setup that we use to perform the dispersive readout of the Josephson phase qubit. In the first part we report about the dc electronics which in this setup are necessary to supply the flux bias to SQUID and to the qubit. In contrast to the readout electronics described before in section 4.3.2, now there is no dc bias directly

applied to the SQUID. Therefore there is no need for the components that were used for preparation of the current ramp, the monitoring of the SQUID voltage, the triggering on the switching events and time counter which are indicated by the red dashed line in Fig. 4.10.

#### 4.4.1 DC electronics

Additionally to the flux control electronics mentioned in section 4.3.2, and indicated in Fig. 4.10 by the blue dashed line, to tune the qubit flux bias, a fourth DAC channel is used to control an extra current source which supplies the flux bias for the dc-SQUID. This flux line is equipped with a current divider and an RC type low pass filter at the 1K pot stage with a cut-off frequency of 10 kHz. At the sample holder, a new type of powder filter [LU08] is installed.

#### 4.4.2 Microwave electronics setup

The microwave setup for the dispersive readout has been newly designed for our qubit experiments. So far, microwave signals were only used to manipulate the qubit, but not for the readout. For the qubit manipulation, a signal is only sent from the room temperature setup down to the qubit in the cryostat. For this one way transmission, a frequency dependent coupling strength of the signal to qubit would be the main problem, which however could be solved relatively easy by readjusting the output power of the microwave source at room temperature.

To use in addition a readout process based on microwave signals makes it necessary to transmit the signal containing the information about the qubit state back from the bottom of the cryostat to the room temperature electronics. The readout SQUID and the qubit can not be protected from thermal noise in this line by just installing large attenuation, as it is done in the downward line. Instead, one has to use a series of cryogenic isolators together with appropriate filters. This will protect the readout system and the qubit from thermal and high frequency noise, but on the other hand, a narrow band is kept open in the frequency spectrum where the very weak signal reflected

from the SQUID resonator can pass to a cold amplifier at 4K. These additional components will always have small impedance mismatches and will therefore introduce extra reflections which will influence the amplitude and phase of the weak measurement signal. So one has to carefully design the path of the microwave to avoid unwanted contributions to the signal. In the following paragraph we describe our microwave setup. The written description is supported by several figures. Figures 4.11, 4.12 and 4.13 show a schematic of the microwave components installed in the dilution refrigerator. Each figure is accompanied by a photograph of a certain section of the low temperature microwave setup. The photograph in Fig. 4.11 shows the mixing chamber plate with the nut to which the sample holder will be screwed. In the back the cryogenic circulator is visible which is attached to the cold plate by a copper fixture. On the left side, four SMA sockets are located which serve for applying fast microwave and dc-pulses to the qubit. On the right side seven MCX sockets are placed to supply the necessary currents for on-chip flux lines.

The photograph in Fig. 4.12 shows the mixing chamber plate, now with the sample holder, magnetic shielding and all dc and microwave lines carefully installed and fixed.

The photograph in Fig. 4.13 shows the top of the inner vacuum chamber (IVC) flange, where a copper plate is installed. A cold amplifier which can be seen on top, is attached to this plate together with a cryogenic circulator below. One port of the circulator is terminated by a  $50\ \Omega$  and serves here as an isolator to protect lower temperature stages from the thermal noise of the amplifier and increases the isolation of the amplifier for room temperature thermal noise. During operation of the cryostat this whole part will be immersed in the Helium bath.

For the frequency domain measurements performing the spectroscopy of the SQUID resonator, a vector network analyzer (VNA) (Agilent E5071C) was used, and the according measurement data are shown in section 5.3.1. For the time resolved measurements, including the measurements of coherent oscillations between the qubit states which are shown in 5.3.2, a different setup, schematically shown in Fig. 4.14 is used.

All microwave components shown in Fig. 4.14, besides the microwave

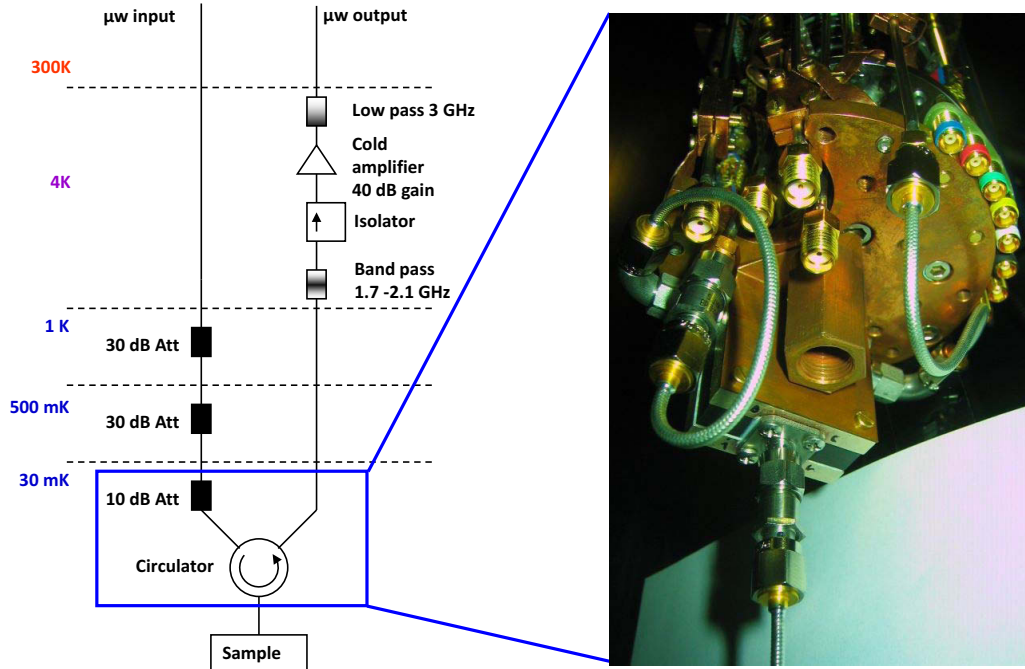


**Figure 4.11:** Schematic of the microwave setup inside the dilution refrigerator. Attenuators are installed on the input line at several temperature stages to reduce the room temperature thermal noise. A cryogenic circulator is installed at the mixing chamber cold plate. A cold amplifier is placed at the 4 K stage which will be immersed in the Helium bath. The photograph shows the mixing chamber plate with the cryogenic circulator and flexible microwave cables installed for a test of all microwave components at room temperature.

source, are arranged on a custom made microwave board, shown in Fig. 4.15. This board serves for a reliable ground connection between the different components and at the same time minimizes the phase fluctuations which would be additionally introduced by accidental bending of the microwave cables.

Now, the microwave signal path will be explained in detail for the measurements involving the microwave board, shown in Fig. 4.15.

The microwave signal for measuring the resonance frequency of the SQUID resonator is generated by a commercially available synthesizer (Anritsu MG37020A) which is controlled by the measurement computer via

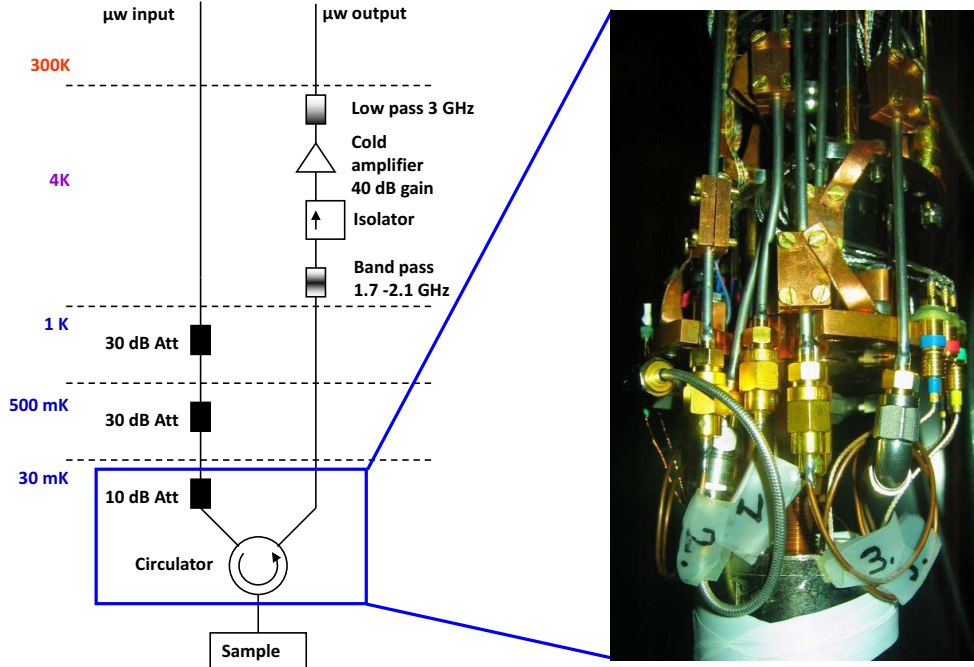


**Figure 4.12:** Schematic of the microwave setup inside the dilution refrigerator, as shown in Fig. 4.11. The photograph shows the mixing chamber, now with the sample holder and magnetic shielding attached, and all microwave and dc lines prepared just before closing the inner vacuum chamber.

GPIB (General Purpose Interface Bus). The continuous wave output signal of the source is split into two parts with equal amplitude and phase by a power divider (Pasternack PE2011). One part is used as a reference signal with respect to phase and amplitude and is directly fed into the local oscillator (LO) input of an IQ-mixer (Marki IQ1545LMP), which we later will refer to. The probe signal passes through a manually adjustable phase shifter (Pasternack PE8247) and is amplitude-modulated by means of two mixers (Mini-Circuits (MC) ZX05-C24LH-S+) connected in series in order to achieve a large on-off ratio of about 64 dB. The modulation signal coming from the second channel of a pulse generator (Agilent E81130) is split by a power divider (Pasternack PE2008) and fed into the IF inputs of both mixers. The pulsed signal passes through a manual step attenuator (Narda 4745-69)

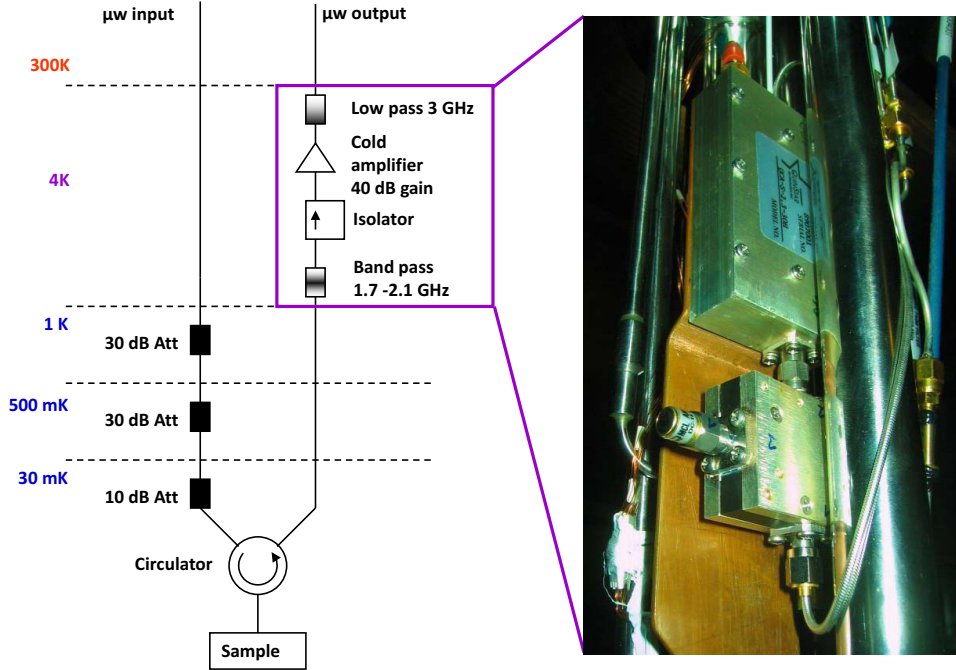


**Figure 4.13:** Schematic of the microwave setup inside the dilution refrigerator, as shown in Fig. 4.11. The photograph shows the 4K stage of the dilution refrigerator, with the cold amplifier on top and a cryogenic circulator below, here used as an isolator with a  $50 \Omega$  load at one port.

and a 40 dB fixed attenuator (Mini-Circuits) to set the proper power level for the experiment before it enters on top of the cryostat.

Inside the cryostat, the signal is attenuated by 70 dB in total using 30 dB attenuators at the 1K pot stage and the 500 mK stage and a 10 dB attenuator at 30 mK. The signal is then passed through a cryogenic circulator (Pamtech STE1438K) with isolation of 18 dB in the frequency range between 1.9 GHz and 2.4 GHz. From there, the signal is guided to the sample holder by a flexible microwave cable and further to the SQUID circuit by an on-chip coplanar transmission line. Two additional 1 dB attenuators, one at the circulator and one at the sample holder, serve for reduction of reflections due to mismatches at the transitions from the cable to the sample holder and further to the chip. Measurements showed that reflections reach

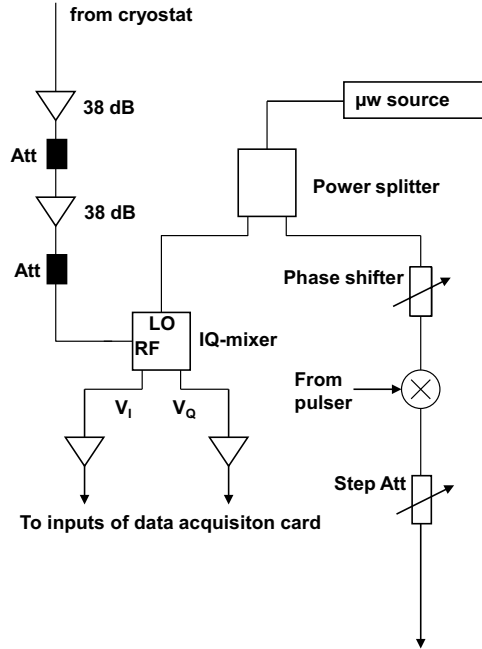


**Figure 4.14:** Schematic of the microwave electronics of the room temperature setup. The signal from the source is split into the reference signal passed to the LO input of the IQ-mixer, and the probe signal passed through the phase shifter, the mixer for pulsing (here only one shown) and the step attenuator, before it enters the cryostat. The reflected signal is amplified and passed to the RF input of the IQ-mixer.

a minimum with the attenuators in this configuration, in contrast to having only one larger attenuator at just one end of the cable, either at the circulator or at the sample holder. For all attenuators used at low temperatures it is crucial to assure that they are not changing their characteristics by becoming superconducting. Here we use attenuators of the Type 18AH from Aeroflex/Inmet [Aer].

The signal reflected by the sample returns to the circulator towards a cold amplifier installed at the 4 K stage, designed for a 42 dB gain at a noise temperature of 6 K (Quinstar QCA-S.3-30H). A narrow-band isolator, installed on the input of the amplifier together with a filter (Mini-Circuits VBFZ-2130) having its pass band between 1.7 GHz and 2.4 GHz, serves

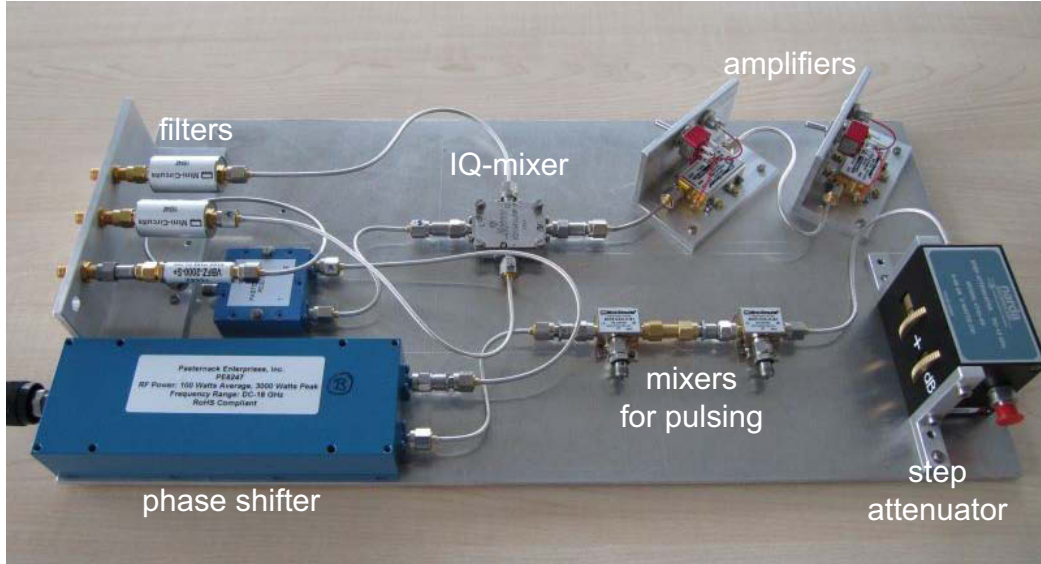


**Figure 4.15:** Custom made microwave board, used to generate the pulsed probe signal for the SQUID resonator, and to determine the change in amplitude and phase of the reflected signal by means of the IQ-mixer.

to protect the sample from the noise of the amplifier. At the output of the amplifier, a low-pass filter (Mini-Circuits VLF-3000) with a cut-off frequency of 3 GHz protects the amplifier and the whole system from high frequency noise.

At room temperature, the signal is amplified by two amplifiers (Mini-Circuits ZX60-2534M) of 76 dB total gain and mixed with the reference signal in an IQ mixer (Marki IQ1545LMP). The  $I$  and  $Q$  outputs of this mixer are determined by a combination of the phase and amplitude of the reflected signal with respect to reference signal. They are low pass filtered to avoid high frequency noise leaking through the mixer and amplified by a low-noise amplifier (SRS SR560) each, which are able of handling pulsed signals. Finally both signals are digitized by means of an 8-bit, 100 MS/s data acquisition card (Spectrum M2i.2030).

Fig. 4.16 shows a schematic of an IQ-mixer which is now going to be explained.

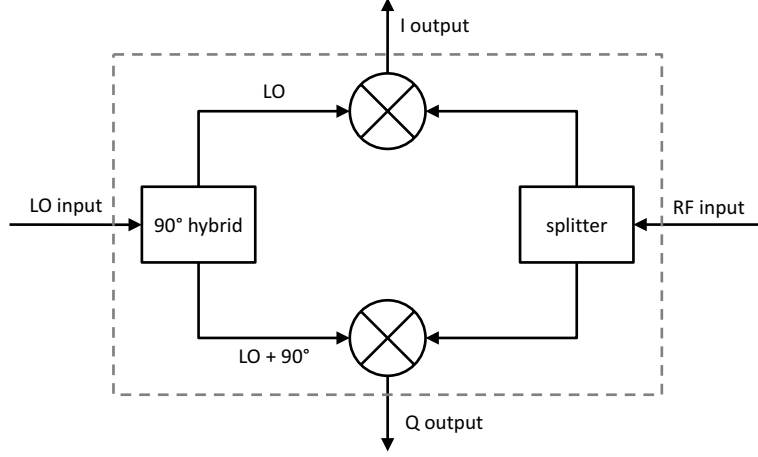


**Figure 4.16:** Schematic of an IQ-mixer, consisting of a power splitter, two mixers and a  $90^\circ$  hybrid, which splits the input signal and shifts the phase by  $90^\circ$  in one branch.

Let us consider a sinusoidal signal with a constant amplitude  $V_0^{LO}$  and frequency  $\omega$  from the synthesizer as local oscillator (LO) input to the IQ-mixer

$$V^{LO} = V_0^{LO} \sin(\omega t), \quad (4.5)$$

and a signal having the same frequency but different amplitude and shifted in phase by  $\alpha$  as the reflected signal from the SQUID resonator at the radio frequency input (RF) to the IQ-mixer

$$V^{RF} = V_0^{RF} \sin(\omega t + \alpha). \quad (4.6)$$

The output voltage  $V^I$  is then given by the product of these two input signals

$$V^I = V_0^{LO} \cdot V_0^{RF} \cdot K \cdot \sin(\omega t) \sin(\omega t + \alpha), \quad (4.7)$$

where  $K$  is a mixer constant including the typical conversion loss. The output

voltage  $V^Q$  is also given by the product taking into account the phase shift of the LO signal,

$$V^Q = V_0^{LO} \cdot V_0^{RF} \cdot K \cdot \sin(\omega t + \pi/2) \sin(\omega t + \alpha). \quad (4.8)$$

This yields

$$V^I = V_0^{LO} \cdot V_0^{RF} \cdot K \cdot \frac{1}{2} [\cos(-\alpha) - \cos(2\omega t + \alpha)], \quad (4.9)$$

and

$$V^Q = V_0^{LO} \cdot V_0^{RF} \cdot K \cdot \frac{1}{2} [\cos(\pi/2 - \alpha) - \cos(2\omega t + \pi/2 + \alpha)]. \quad (4.10)$$

For both voltages the oscillating term is now going to be neglected which is taken care of in the measurement by low pass filtering both signals.

$$V^I = V_0^{LO} \cdot V_0^{RF} \cdot K \cdot \frac{1}{2} \cos(-\alpha) = V_0^{LO} \cdot V_0^{RF} \cdot K \cdot \frac{1}{2} \cos(\alpha), \quad (4.11)$$

$$V^Q = V_0^{LO} \cdot V_0^{RF} \cdot K \cdot \frac{1}{2} \cos(\pi/2 - \alpha) = V_0^{LO} \cdot V_0^{RF} \cdot K \cdot \frac{1}{2} \sin(\alpha). \quad (4.12)$$

Taking into account that the amplitude of the incident signal  $V_0^{LO}$  is considered to be constant, one can define a new constant  $K' = \frac{1}{2} \cdot V_0^{RF} \cdot K$  and gets

$$V^I = V_0^{RF} \cdot K' \cos(\alpha), \quad (4.13)$$

and

$$V^Q = V_0^{RF} \cdot K' \sin(\alpha). \quad (4.14)$$

One can see that  $V^I$  is proportional to the real part of the complex signal while  $V^Q$  is proportional to the imaginary part of the complex signal with amplitude  $R = V_0^{RF} \cdot K'$  and the phase  $\alpha$  which are given by

$$R = \sqrt{(V^I)^2 + (V^Q)^2}, \quad (4.15)$$

and

$$\alpha = \arctan\left(\frac{V^Q}{V^I}\right). \quad (4.16)$$

This setup allows for recording the  $I$  and  $Q$  data and to calculate the amplitude and phase of the reflected microwave signal for each measurement point during a sweep in frequency and applied magnetic flux. The measurements are shown in section 5.3.1 related to the characterization of the SQUID.

Then, for the qubit readout, the SQUID is only probed at a fixed frequency. For these measurements which are shown in section 5.3.2 the phase shifter mentioned above is used to adjust the phase of the signal in the measurement loop in a way so that one of either  $I$  and  $Q$  signals becomes zero and the other one reaches a maximum for the chosen frequency. This allows for a maximal readout contrast while only occupying one channel of the data acquisition card and leaving the second channel for future experiments involving a second SQUID resonator coupled to second qubit.

A pulse generator (Agilent E81130) which is controlled by the measurement computer via GPIB is used to create a proper pulse sequence to control the qubit manipulation and the readout of the SQUID. The trigger signal for the analog flux control electronics, the pulse modulation for SQUID microwave signal and the trigger signal for the data acquisition card are directly supplied by this generator. Additionally it triggers an arbitrary waveform generator (Tektronix AWG7062B) which is used because of its better time resolution and its versatility with respect to the pulse shape to generate the microwave and the flux pulse for the qubit.

The qubit microwave line and the qubit flux line are realized by two semi-rigid coaxial cables. Each line has a 20 dB attenuator installed at the 500mK stage and another 10 dB at the 30mK cold plate.

Figure 4.17 shows the phase qubit operation cycle for the dispersive readout scheme in contrast to the operation cycle of the switching current readout shown in Fig. 2.12. The initialization by the flux bias and the qubit operation by the applied microwave pulse are explained in section 2.3.1. Here one qubit operation cycle takes only 100  $\mu s$  including 20  $\mu s$  for setting the flux back to the initialization level. The actual measurement time of the SQUID here is only 24  $\mu s$ .

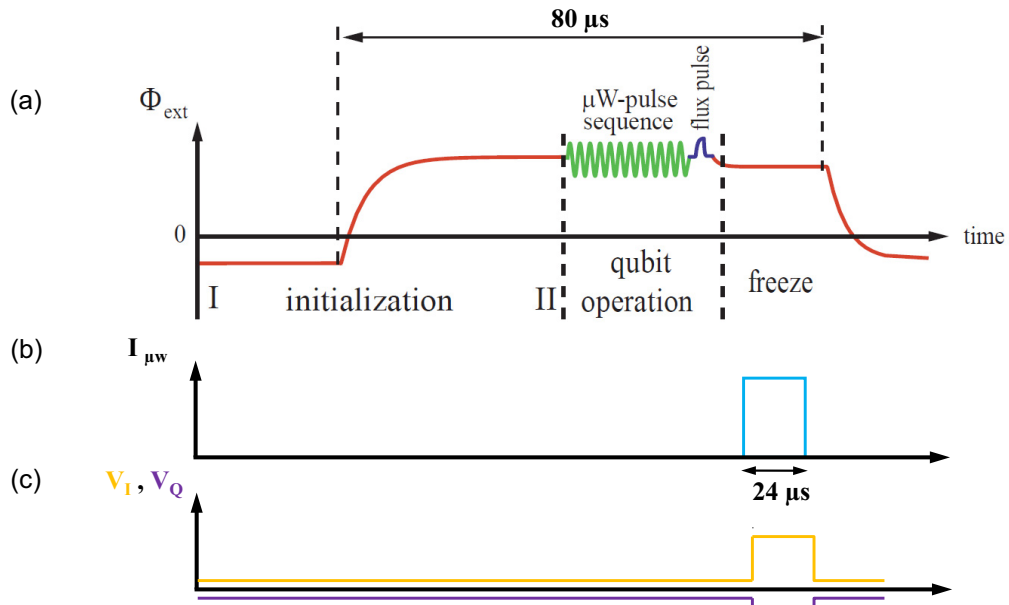


**Figure 4.17:** One operation cycle of the phase qubit with the dispersive readout. (a) The red line shows the time dependence of the flux which is applied to the qubit. (b) The light blue line shows the pulsed microwave probe signal that is applied to the SQUID resonator. (c) The orange and the purple line show the output voltages  $V_I$  and  $V_Q$  respectively of the IQ-mixer. The time line is not to scale.



# Chapter 5

## Measurement Results

In this chapter we are going to present the results of the measurements that were performed on the samples described in section 4.1 by using the different measurement setups shown in chapter 4. We start with a section about the measurements done at 4K with the low temperature laser scanning microscope (LTLSM) setup described in section 4.2 for a first characterization of our resonators.

The measurements were then continued in a  $^3\text{He} / ^4\text{He}$  dilution cryostat at a base temperature of 30mK. Two different electronic setups have been used for the SQUID switching current readout of the qubit on the one hand, and the dispersive readout on the other hand which are described in sections 4.3 and 4.4 respectively.

### 5.1 LTLSM Measurements

In the following section we show measurement results that were obtained by probing the resonator with a laser beam while it is at a temperature of 4K in the LTLSM cryostat and supplied with a microwave signal. The measurement setup and technique are described in section 4.2. This method allows for extracting  $J_{\mu\text{w}}^2(x, y)$  maps ([CNW98]) from the microwave photo response according to the signal generation model in section 4.2.

Additionally, the optical contrast mode of the LTLSM was used for mapping the results of the microwave photo response mode to the actual

sample layout. Figure 5.1 shows an image of a resonator which was recorded by measuring the reflectivity of the sample. The resonator is formed by a loop that is shunted by a capacitor. This specific design is similar to the sample layout shown in Fig. 4.1, but does not contain Josephson junctions. It is designed for probing only the LC resonance of the structure.

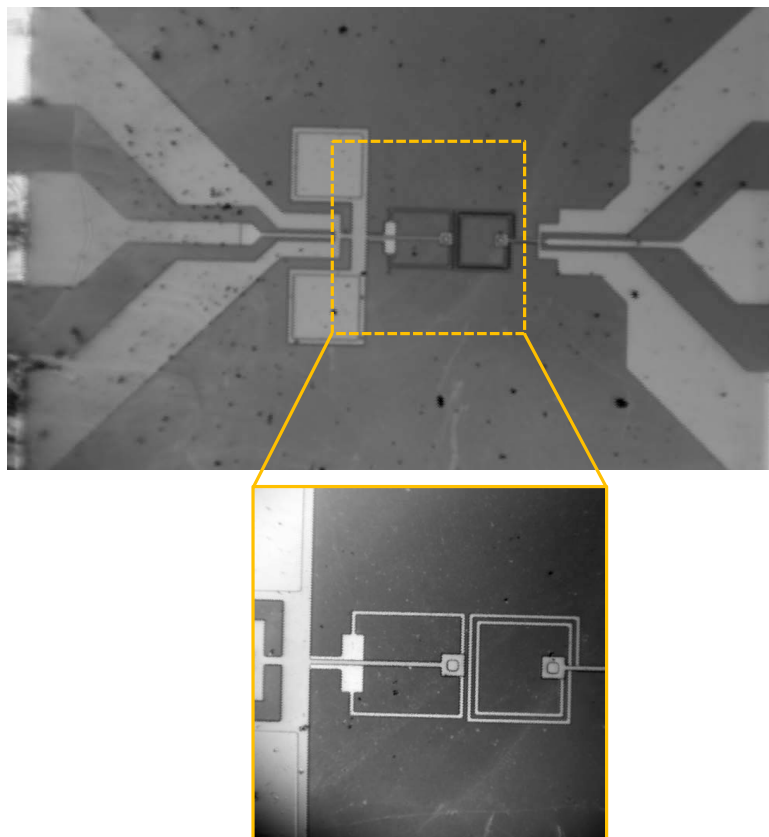


**Figure 5.1:** Micrograph of an LC resonator obtained by recording the reflectivity of the structure in the optical contrast mode of the LTLSM. The structure does not contain Josephson junctions, it is a plain lumped element LC-resonator.

Figure 5.2 shows a micrograph obtained with the LTLSM in the optical contrast mode of the sample containing Josephson junctions depicted in Fig. 4.1.

In the following figures we will present the measurement results which

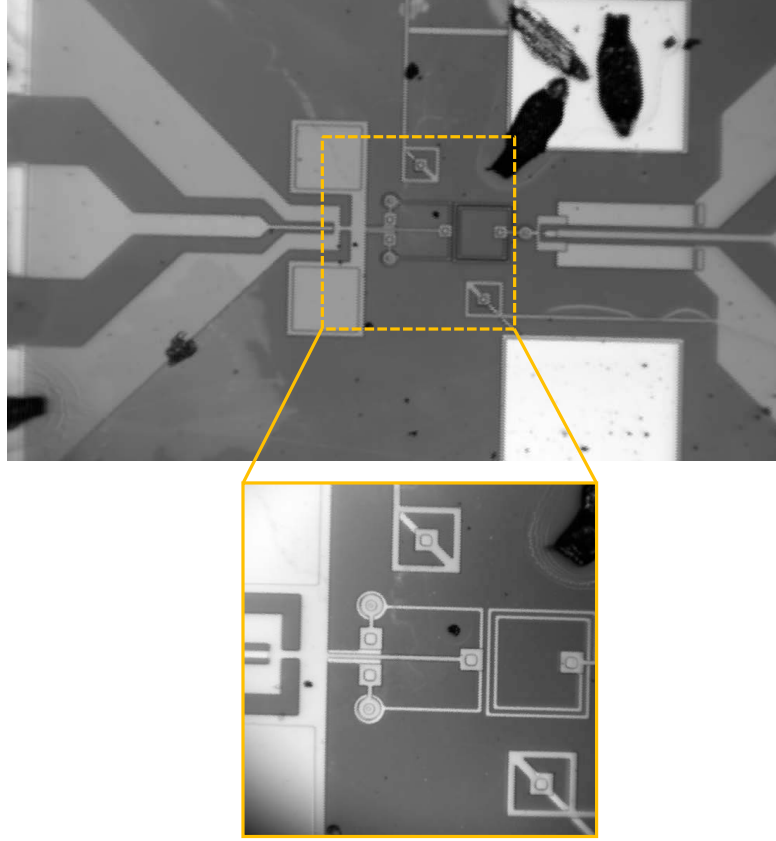


**Figure 5.2:** Micrograph of the SQUID resonator, on the left, and the qubit on the right, obtained by recording the reflectivity of the structure in the optical contrast mode of the LTLSM.

were obtained for both these samples mentioned before, by using the LTLSM setup in the microwave photo response mode, as described in section 4.2.

Figure 5.3 shows the local microwave photo response of the LC-resonator without Josephson junctions versus the spatial coordinates  $x$  and  $y$ . This measurement was recorded while a continuous microwave signal at  $f = 2.85$  GHz was applied to the sample. The signal level is encoded in color and shows a homogeneous distribution along the center conductor and in the two branches of the loop.

To see the resonance of the structure in the frequency domain, we

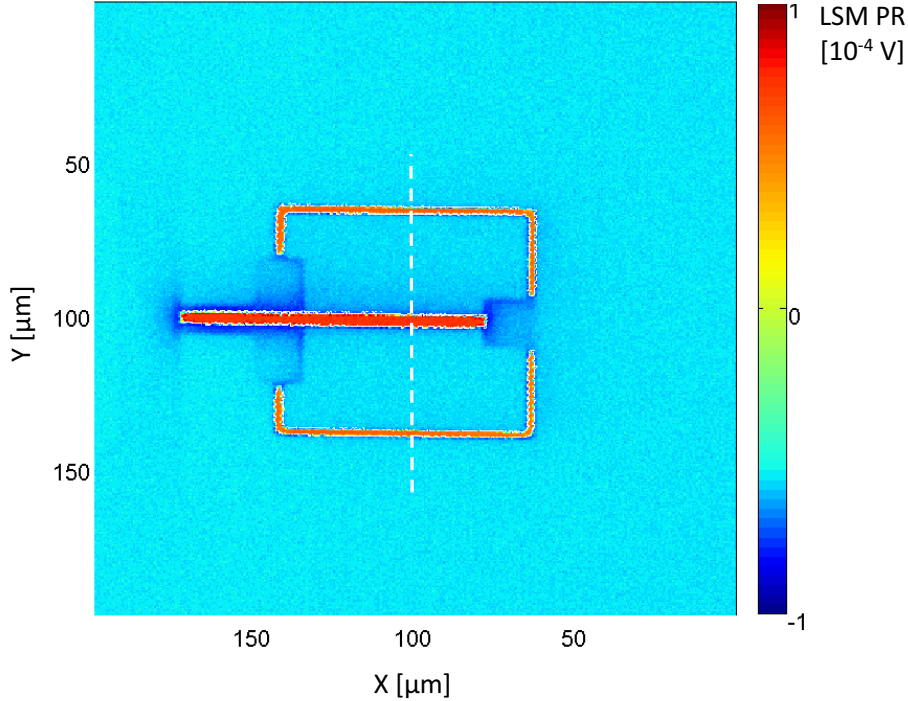


**Figure 5.3:** LTLSTM microwave photo response (color-coded) of the LC resonator without Josephson junctions. The resonator is excited with a microwave signal at its expected resonance frequency  $f_{LC} = 2.85$  GHz, which is fed to the structure from the left.

restrict the scan area for next measurement to a narrow line across the center conductor of the resonator and the two branches of the loop. This cross section is indicated in Fig. 5.3 by a white dashed line at  $x = 100 \mu m$ . The illuminated spot is scanned just along this line while for each scan the microwave frequency that is applied to the resonator is increased step by step. After performing each of these measurements and merging them into one file, one gets the frequency dependence of the microwave photo response. The obtained data are shown in Fig. 5.4. The measurement reveals the largest microwave photo response at the resonance frequency  $f_{LC} = 2.85$  GHz in the center conductor and in the two branches of the loop. One can also

notice side minima and maxima appearing for lower and higher frequencies. These are attributed to the microwave setup that was used to access the broad frequency range from 1.5 GHz to 4.5 GHz and which is shown in Fig. 4.7. As already mentioned there, a kind of bypass for the microwave signal was necessary to bias the diode detector close to its working point, since the microwave signal reflected from the sample was too weak. Just before the diode, both signals were combined. Due to the different path lengths in the microwave setup cabling and the phase difference occurring therefore, the measurement data were overlaid with an interference pattern which can be seen in Fig. 5.4.

Since for the measurement data shown in Fig. 5.4 the x-coordinate of the scan has already been set to a fixed value, one can now extract the microwave photo response versus frequency dependence at a specific point of the resonator structure by choosing a certain value of the y-coordinate. This is done by having a look at the cross section of measurement data shown in Fig. 5.4 for a fixed value of  $y = 49\mu m$ . Figure 5.5 shows the microwave photo response for the single point  $(x = 100\mu m, y = 49\mu m)$  in the middle of the center conductor of the loop. Due to a change of the scan step size this corresponds to the point  $(x = 100\mu m, y = 100\mu m)$  in Fig. 5.3. Figure 5.5 clearly reveals the interference pattern, overlaying the expected microwave photo response. The inset of Fig. 5.5 shows a 165 MHz wide spectrum, where in the central part, the photo response is not dominated by the interference. There, the measured signal is in qualitative agreement with the signal generation model, shown in section 4.2, and the shape of the curve compares to Fig. 4.5(b).

The analysis of the LC resonator circuit by means of the LTLISM technique revealed the resonance frequency of the structure at  $f_{LC} = 2.86$  GHz. The obtained results are nicely illustrated by Fig. 5.3 and Fig. 5.4.

A further experiment, done with LTLISM, was the investigation of the SQUID resonator, consisting of the loop, the Josephson junctions and the shunt capacitors, as shown in Fig. 4.1 and Fig. 5.2. Compared to the LC resonator investigated before, the additional Josephson inductance introduced by the junctions will reduce the resonance frequency of the structure to the range below 2.1 GHz, actually depending on the externally applied

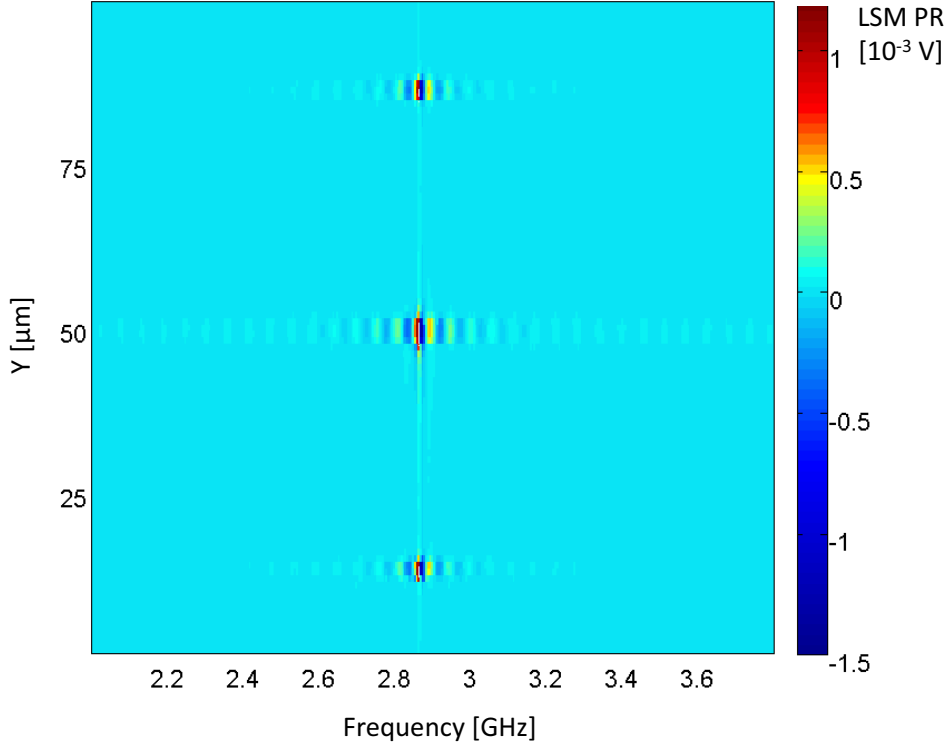


**Figure 5.4:** Microwave photo response versus the excitation frequency and the spatial coordinate  $y$ , corresponding to a line scan at  $x = 100\mu m$  in Fig. 5.3. The largest response in the center conductor and the two branches of the resonator loop is shown at a frequency  $f = 2.85$  GHz. The response is overlaid by an interference pattern which is explained in the text. The three spots at 2.85 GHz correspond to the lower and upper branch, and the center conductor of the resonator loop respectively.

magnetic flux, as it is explained in section 3.1. The experiment was carried out in the same way as it is described before in this section for the LC resonator. Figure 5.6 shows the microwave photo response for the SQUID resonator measured with the LTLISM setup.

The measurements showed that no distinct resonance point could be detected for SQUID resonator, as compared to the measurement of the LC

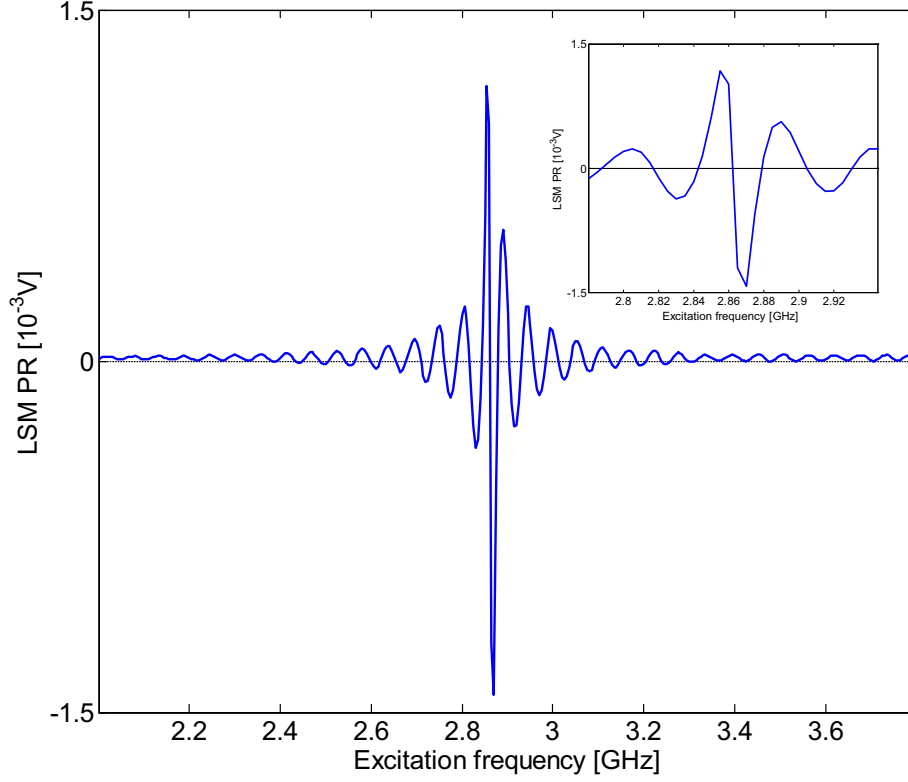


**Figure 5.5:** Microwave photo response versus the excitation frequency applied to the resonator. The curve shows the measured data points for a fixed value of  $y = 49\mu\text{m}$  of the measurement shown in Fig. 5.4. The inset shows a magnification of a 165 Mhz wide spectrum, centered around 2.86 Ghz.

resonator, shown in Fig. 5.4. Despite the fact that the measurements also showed the interference pattern, introduced by the setup, there was no signature of a resonance visible. The reason for this was attributed on the one hand to the electromagnetic rf-noise in the environment which can enter the cryostat through the optical window for the laser. The electromagnetic noise suppresses the critical current of the SQUID which was verified by a switching current measurement while the sample was installed in the LTLSM cryostat. On the other hand, additional thermal noise from the room tem-

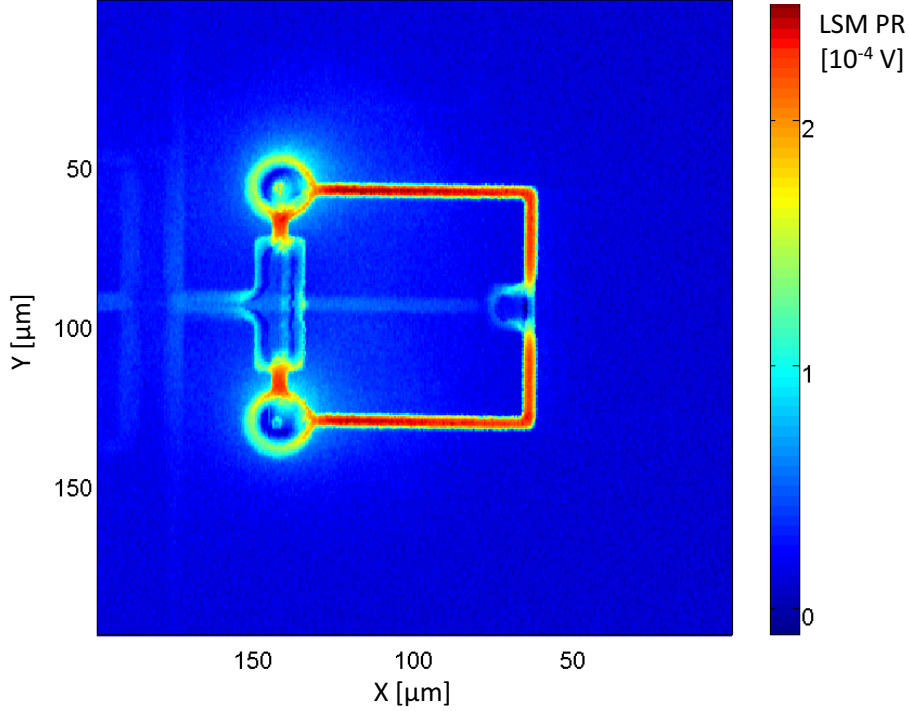


**Figure 5.6:** LTLSM microwave photo response of the SQUID resonator at an excitation frequency  $f = 1.925$  GHz and a microwave power  $P_{\mu w} = -60$  dBm.

perature setup was also introduced by the microwave line attached to the SQUID. Therefore it can not be excluded that the noise current exceeded the critical current of the SQUID and lead to a complete attenuation of the resonance. For future measurements the problem of the thermal noise entering via the the microwave line could be cured by installing a cryogenic circulator inside the LTLSM cryostat.

Only after finishing the experiments with the LTLSM, we had an idea, how to avoid the interference pattern introduced by the additional bias needed to operate the detector diode at the working point, as it is explained in section 4.2. The alternative would be, to use a bias-tee to supply an additional dc-bias to the diode instead of an rf-bias which is responsible for the

interference.

## 5.2 Switching current measurements

In this section we are presenting the measurement results obtained by reading out a phase qubit in the conventional way, by measuring the switching current statistics of a dc-SQUID inductively coupled to the phase qubit. The setup for this kind of readout is described in section 4.3. The measured circuit contains a Josephson phase qubit with the same parameters given in section 4.1.

In contrast to the symmetric dc-SQUID which is used for the dispersive readout, the conventional readout typically uses a three junction asymmetric dc-SQUID. The symmetric dc-SQUID contains two Josephson junctions of the same size, and therefore of the same critical current. The asymmetric dc-SQUID contains three junctions. While two of them are put in series in one branch of the loop, the third junction, having a larger critical current is placed in the other branch of the loop. A more detailed explanation of the asymmetric dc-SQUID is given in [Lis08] and in [Wir06]. There, also the switching current readout is explained in more detail, which allows to record the switching currents statistics of the dc-SQUID.

After mapping the qubit states to distinct flux states in neighboring wells of the qubit potential, as described in section 2.3, the switching current statistics of the dc-SQUID are recorded. This measurement is shown in Fig. 5.7. There, one peak of the histogram corresponds to the qubit being detected in the ground state, while the second peak corresponds to the qubit being detected in the excited state.

By setting a threshold current at the overlap point of the histograms, the measured switching current statistic is mapped to the escape probability  $P_{\text{esc}}$  of the first excited qubit state from the shallow to deep potential well. The probability  $P(|1\rangle)$  of qubit being measured in the excited state is thereby defined as  $P(|1\rangle) = P_{\text{esc}}$ .

By doing microwave spectroscopy on the qubit, the dependence of the qubit resonance frequency, corresponding to the energy level splitting between the qubit states, and the externally applied flux is found.

The qubit is then biased at a certain flux and excited by a microwave

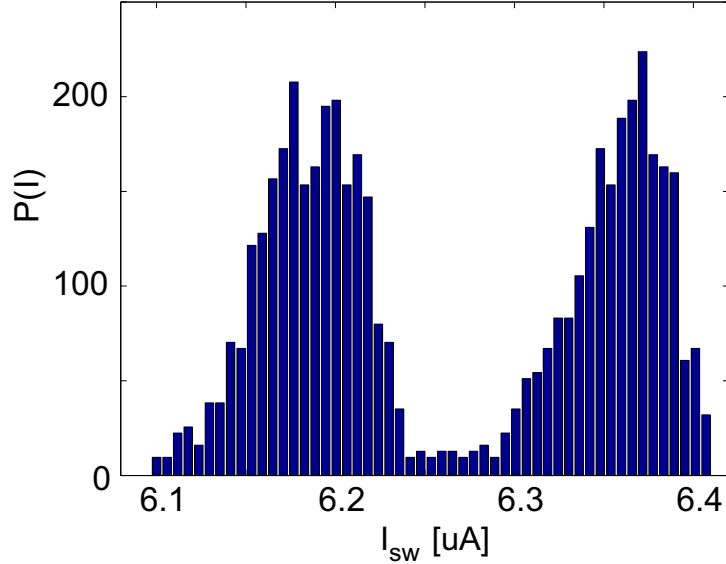


**Figure 5.7:** Switching current histograms of the readout dc-SQUID for two different flux states of the qubit.

signal of according frequency, as illustrated by Fig.2.12. This perturbation introduces coupling of the ground and first excited state of the qubit and drives coherent oscillations between the states, as explained in section 2.3.2. The Rabi oscillations of the measured qubit are shown in Fig. 5.8 for three different powers of the applied microwave. The frequency of the oscillations (Rabi frequency) depends on the applied microwave current, and therefore the applied microwave power according to Eq. (2.51).

The energy relaxation time  $T_1$  as well as the dephasing time  $T_2$  of the qubit, are relevant measures for the actual quality of the qubit. The energy relaxation time  $T_1$  is measured as the decay time of the qubit from first excited state. Therefore a microwave pulse of defined length is applied which is usually referred to as  $\pi$ -pulse. Figure 5.9 shows the energy relaxation time  $T_1$  measurement, where a 1.4 ns long microwave pulse populates the first excited state at time  $t = 0$ .

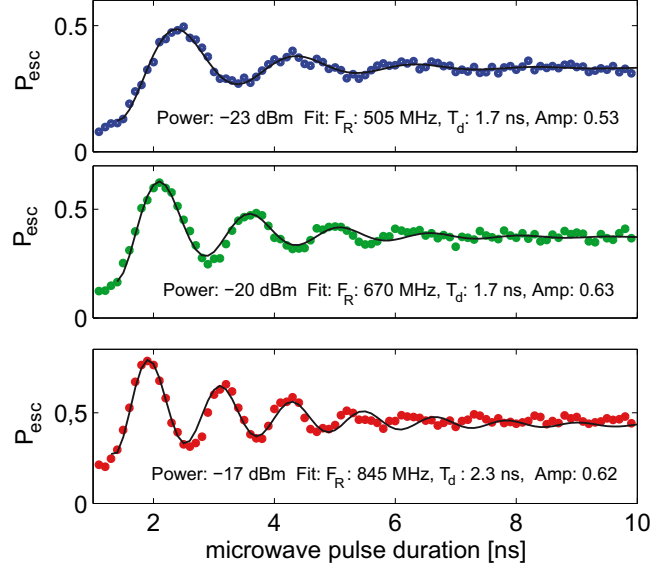


**Figure 5.8:** Coherent oscillations (Rabi oscillations) between the qubit states, measured for three different powers of applied microwave at a frequency of 12.6 GHz. An exponentially decaying  $\sin^2$  is fitted to the measurement data. This reveals a decay time of  $T_d \approx 2$  ns.

### 5.3 Measurements on the dispersive readout

In section 4.3 we showed the standard method ([CSM<sup>+</sup>04, PDP<sup>+</sup>06, CFHB07, LLA<sup>+</sup>07]) to read out a Josephson phase qubit, and showed according measurements done with our setup in section 5.2. The switching of the readout SQUID to its non-superconducting state generates heat directly on the chip and quasi-particles in the circuitry. Both effects are responsible for a relatively long cool-down time of about 1-2 ms that is required after each switching event. This, together with the time needed to ramp up the bias current of the SQUID, limits the repetition rate of the experiment.

To overcome these limitations of the conventional readout, the dispersive readout scheme was introduced in chapter 3. In the following section we present the measurements done on the dispersive readout of the Josephson phase qubit with the setup described in section 4.4 on the sample described

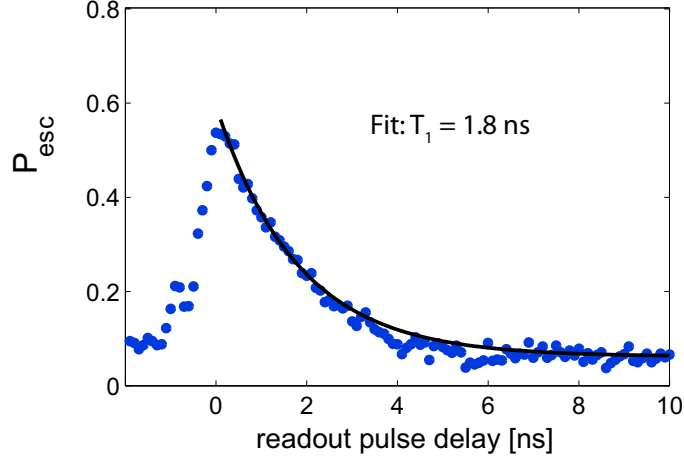


**Figure 5.9:** Measurement of the energy relaxation time  $T_1$  of the first excited state of the qubit. An exponential decay is fit to the measurement data, revealing an energy relaxation time  $T_1 = 1.8$  ns.

in section 4.1

We start with a characterization of the microwave setup installed in our  $^3\text{He}/^4\text{He}$  dilution refrigerator, as shown in Figs. 4.11, 4.12 and 4.13, together with the sample, by performing a transmission measurement with a vector network analyzer (VNA). Further experiments in the frequency domain were then continued by using the IQ-mixer setup shown in Figs. 4.14 and 4.15 instead of the VNA. This setup together with a broad band data acquisition hardware also allowed for time resolved measurements of the qubit evolution, which are concluding this chapter.

### 5.3.1 SQUID detector characterization

The characterization of our microwave setup inside the dilution refrigerator and our sample started with a transmission measurement ( $S_{21}$ ), done by means of a vector network analyzer. This device applies a microwave signal, swept in frequency to the input port of the low temperature microwave setup (see Fig. 4.11) and receives the transmitted signal. Fig. 5.10 shows the according measurement. The absorption dip at 2.08 GHz is attributed to the

resonance of the SQUID resonator. One can further see that the band width of the system is limited to the range between 1.6 GHz and 2.8 GHz, mainly by the band width of the cryogenic circulator, isolator and the additionally installed filters at 4K. Outside this range the signal decreases to the noise level of the VNA. The response between 1.8 GHz and 2.4 GHz is not flat due to the installed filters.

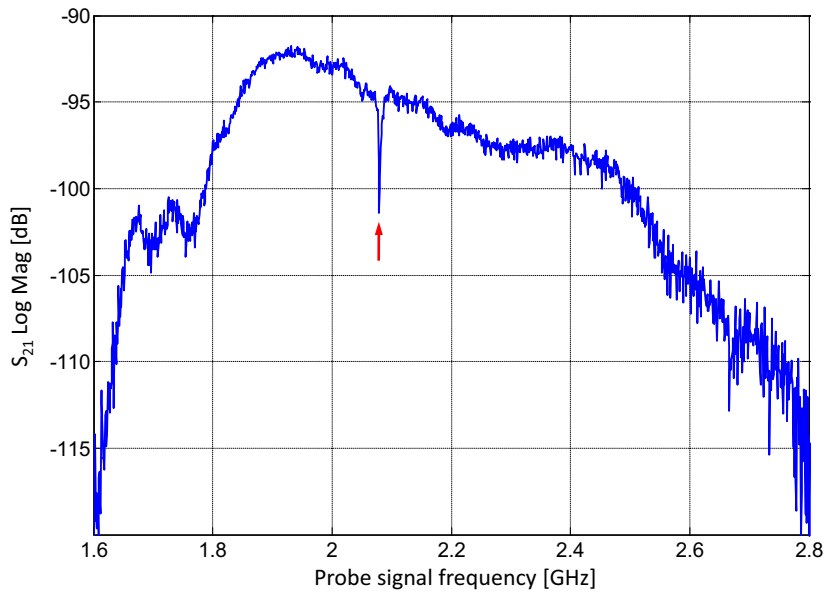


**Figure 5.10:** Measurement, showing the transmission spectrum of the cold setup. The red arrow indicates the resonance frequency of the SQUID resonator  $f_{\text{Res}} = 2.08$  GHz.

As it was described in section 3, the resonance of the SQUID resonator is tunable by an externally applied magnetic flux. For this, the on-chip flux line (see Fig. 4.1), just below the SQUID loop was used. The flux can be adjusted by means of a voltage controlled current source of our custom made dc-electronics. This current source is controlled by the measurement computer, running custom made scripts, based on MATLAB. Figure 5.11 shows the position of the resonance dip in the the spectrum of the applied

frequency as a function of the applied flux. A frequency sweep was recorded for each flux value, as it can be seen for  $\Phi_S = 0$  in Fig. 5.10. Afterwards the position of the resonance dip was extracted from the data. For each flux value, the position of the dip is indicated by a red circle for the flux swept from negative to positive values, and by a blue dot for the flux swept in opposite direction. During each flux sweep, due to crosstalk between the SQUID flux bias line and the qubit loop, approximately one flux quantum  $\Phi_0$  enters or leaves the qubit loop, which gives rise to an abrupt shift of the dip frequency at specific flux bias values. This frequency shift can be observed in Fig. 5.11 at  $\Phi_S = -0.26\Phi_0$  and  $\Phi_S = 0.02\Phi_0$ .

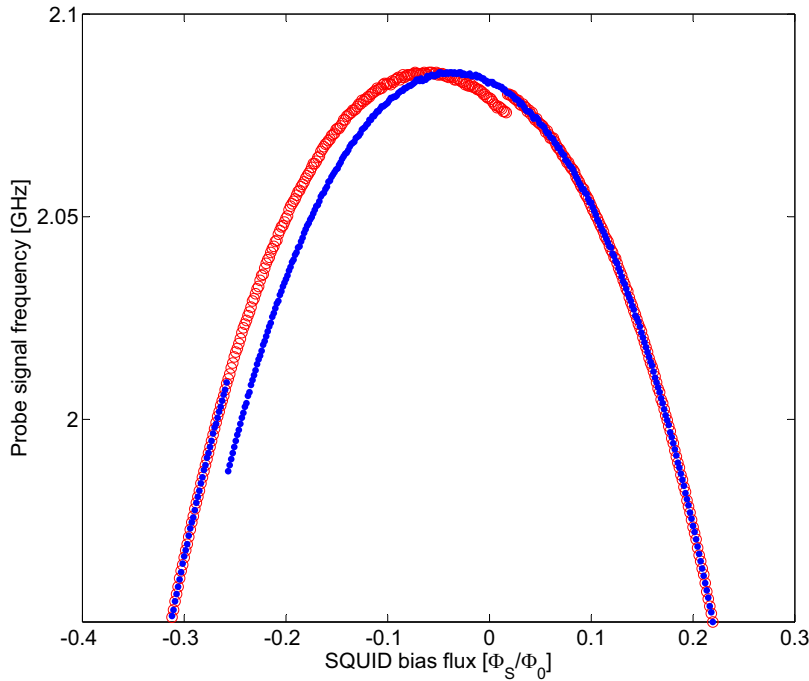


**Figure 5.11:** Resonance frequency of the SQUID resonator as a function of externally applied magnetic flux. Red circles and blue dots show the the positions of the resonance dips as a function of the applied flux, for two different directions of the flux sweep. See text for detailed explanation.

As already mentioned before the band width of the setup was limited, and therefore it was not possible to record a complete period of the flux dependency of the resonance. Since this dependence is known by Eq. (3.7), it was possible to fit it to the data points. These fits together with the measured data points are shown in Fig. 5.12. The solid red line indicates the measurement data for the flux swept from negative to positive values, while the solid blue line indicates the data for the flux swept in opposite direction. The dotted blue line shows the fit to the blue data points on the right-hand side of the step at  $\Phi_S = -0.26\Phi_0$ . The dashed red line displays the fit to the red data points on the left-hand side of the step at  $\Phi_S = 0.02\Phi_0$ .

The fit formula is given by:

$$f_{\text{Res}}(B) = \frac{1}{2\pi \sqrt{\left( L_S + \frac{\Phi_0}{4\pi I_{c0} |\cos(\pi \frac{B+B_{\text{offs}}}{B_0})|} \right) C_1}}, \quad (5.1)$$

where  $B$  is the applied flux in units of the volt, applied to the voltage controlled current source, biasing the flux line.  $B_{\text{offs}}$  is the x-offset of the curve maximum in units of volt, and  $B_0$  is a normalizing factor, relating the voltage scale to the actual flux scale. These three variables are fit parameters, and additionally the loop inductance  $L_S$ , the shunt capacitance  $C_1$  and the critical current of a single Josephson junction  $I_{c0}$ . The yielded values of the fit parameters are in good agreement with the designed values, as they are (design values are given in parenthesis):

Single junction critical current:  $I_{c0} \approx 2 \mu A$  (2.1  $\mu A$ );

SQUID loop inductance:  $L_S \approx 161 \text{ pH}$  (111 pH);

Shunt capacitance:  $C_1 \approx 24 \text{ pF}$  (36 pF);

More over, the shift between the two curves in Fig. 5.12 of  $26 m\Phi_0 = M I_{c0}$ , introduced by a flux jump in the qubit, reveals a mutual inductance between the SQUID loop and the qubit loop  $M \approx 27 \text{ pH}$ , which matches very well to

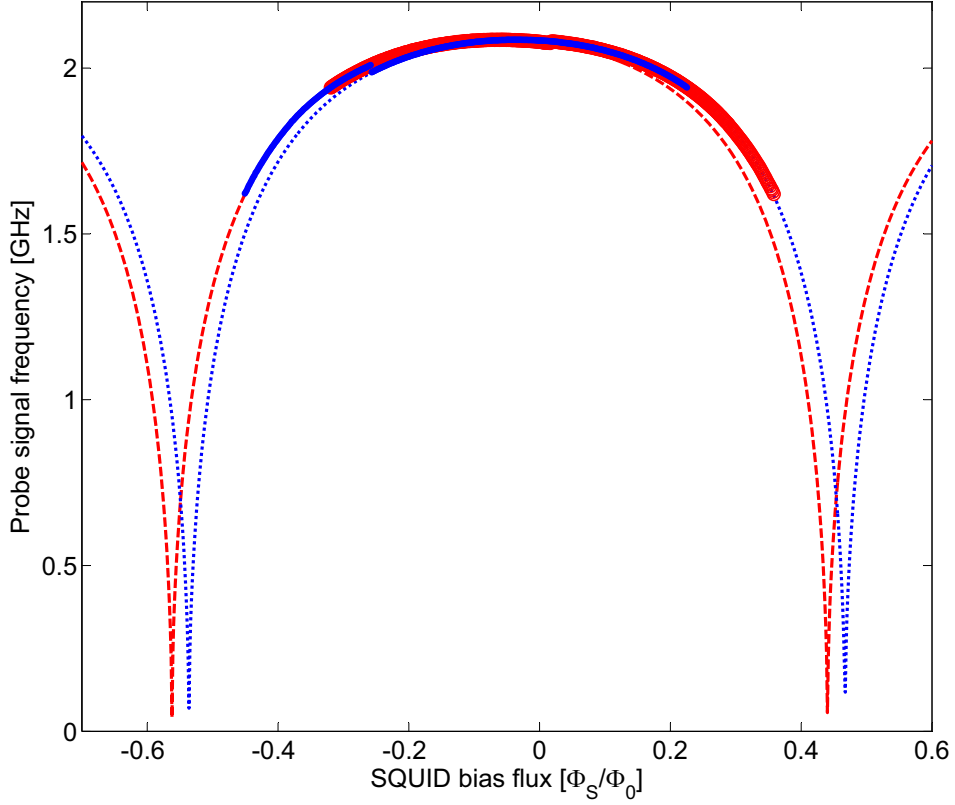


**Figure 5.12:** Resonance frequency of the SQUID resonator as a function of externally applied magnetic flux. The blue solid line and the red solid line correspond to the measurement data, shown in Fig. 5.11. The dashed and dotted lines correspond to fits to the measured data. See text for detailed explanation.

the designed value of  $M = 30$  pH.

Since the measurement speed of the vector network analyzer and its data transfer rate to the measurement computer limit the data acquisition rate, the following measurements are done by using the IQ-mixer setup, shown in Figs. 4.14 and 4.15, instead of the VNA. A broad band data acquisition card in the measurement computer is used to record the output

voltages of the IQ-mixer.

From the recorded values of the IQ-mixer output voltages the signal amplitude can be calculated according to Eq. 4.15. The frequency of the probe signal is swept by the microwave source, supplying the probe signal to the microwave board and further to the sample. The microwave board also allows for pulsing the probe signal in contrast to the VNA which is applying a continuous signal.

As described before for the VNA measurements, again the flux is swept, but now the flux is applied via the qubit flux line, since this configuration is also going to be used later for the time resolved measurements on the qubit. The qubit flux line is shown in Fig. 4.1, above the qubit loop. Due to crosstalk between the qubit flux line and the SQUID loop, the SQUID resonator is also de-tuned by this flux. For each flux value, the probe signal frequency is swept by the microwave source, while the output voltages of the IQ-mixer are recorded. This allows to acquire a frequency spectrum for each flux point. The position of the resonance dip in the spectrum is determined in the same way as described before by a script on the measurement computer. Fig 5.13 shows the positions of the dips with respect to the probe signal frequency, for the flux swept from negative to positive values, while Fig 5.14 shows the position of the dips, for the flux swept in opposite direction. During each flux sweep approximately two flux quanta  $\Phi_0$  enter or leave the qubit loop, each of which gives rise to an abrupt shift of the dip frequency at specific flux bias values. These values are  $0.001 \Phi_0$  and  $0.25 \Phi_0$  in Fig. 5.13, and  $-0.124 \Phi_0$ , and  $0.124 \Phi_0$  in Fig. 5.14, which are indicated by arrows.

The flux jump in Fig. 5.13 at  $\Phi_Q = 0.25 \Phi_0$ , is now going to be further investigated. The SQUID resonator frequency shift induced by the qubit is shown in detail in Fig. 5.15(a). It displays two traces of the normalized reflected signal amplitude versus the applied microwave frequency in the vicinity of qubit-state switching. The left curve, with its minimum at 1.896 GHz corresponds to the lower data point at the respective flux jump in Fig. 5.13, while the right curve, with its minimum at 1.926 GHz corresponds to upper data point. For this measurement, a very low microwave power of -120 dBm was applied to the SQUID to stay in the linear regime, giving rise to the Lorentzian shape of the resonance dips. Taking into account the line

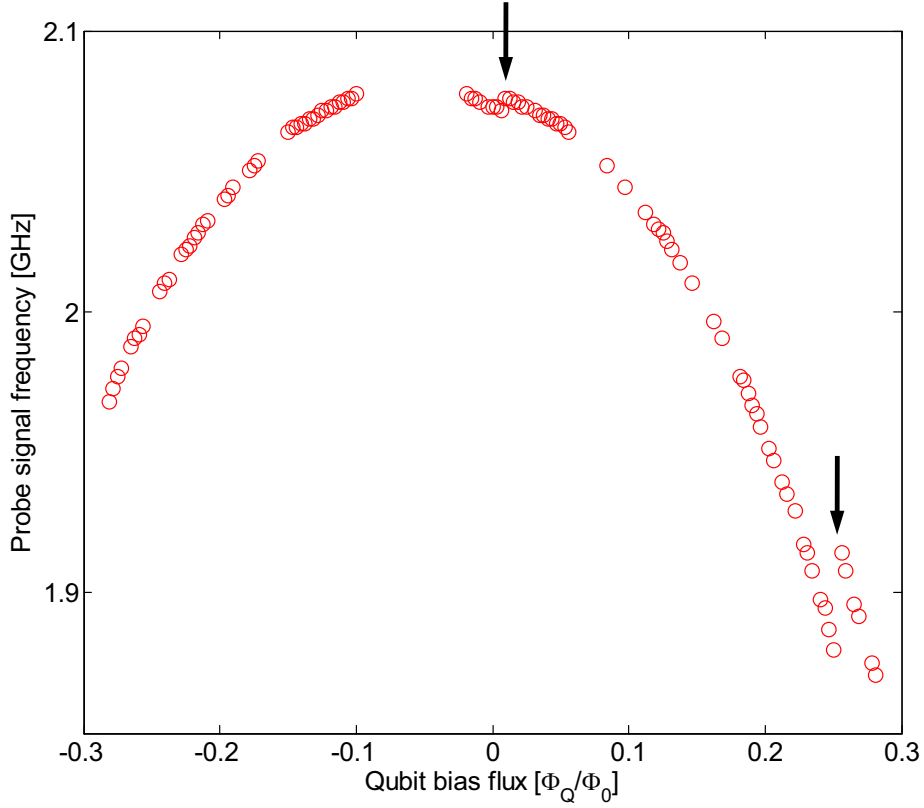


**Figure 5.13:** Resonance frequency of the SQUID resonator as a function of magnetic flux swept upward and applied via the qubit flux line. Each red circle corresponds to the resonance dip at the respective value of flux bias. Arrows indicate flux jumps in the qubit. See text for detailed explanation.

width of 4 MHz and the dependence of the resonance frequency on the flux, a resolution of the detector of 2 - 3  $m\Phi_0$  is achieved at an operating frequency of 1.9 GHz. As the two qubit states differ by a magnetic flux on the order of  $\Phi_0$ , very weak inductive coupling between the SQUID and qubit for future experiments is possible.

Fig. 5.15 (b) shows the same frequency range as above, but now the power of the input signal is larger, -115 dBm, driving the SQUID into the nonlinear regime. This is revealed by the asymmetric shape of the dips, as

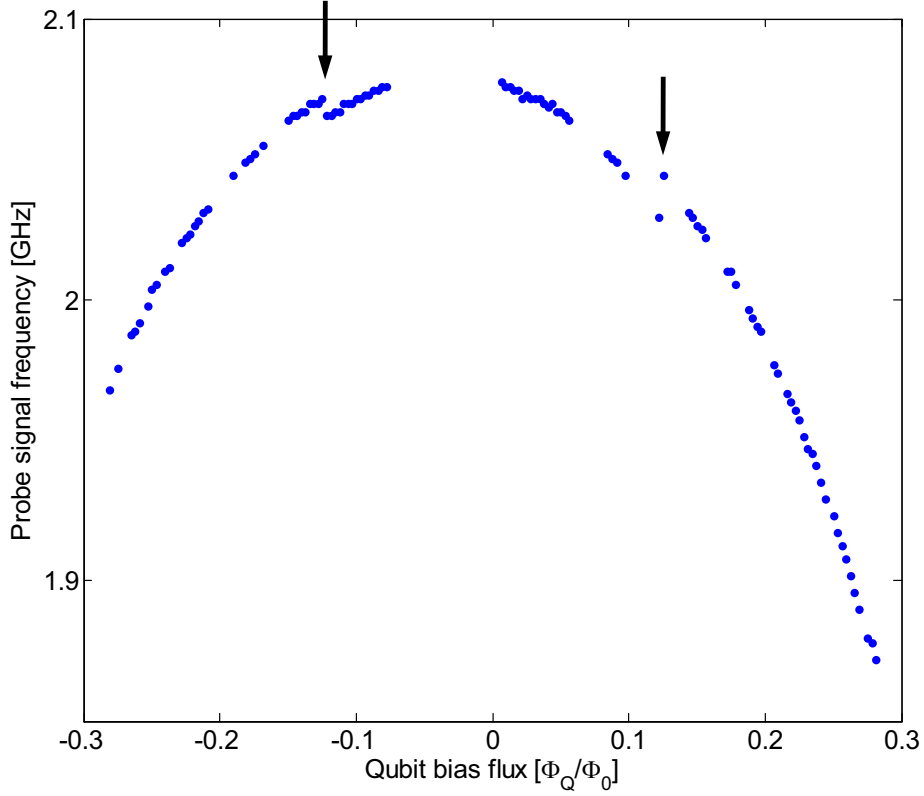


**Figure 5.14:** Resonance frequency of the SQUID resonator as a function of magnetic flux swept downward and applied via the qubit flux line. Each blue dot corresponds to the resonance dip at the respective value of bias flux. Arrows indicate flux jumps in the qubit. See text for detailed explanation.

shown in section 3.2. The advantage of the non-linear regime is the sharper edge on the low-frequency side which allows for an improved flux resolution of about  $0.5 - 0.7 \text{ m}\Phi_0$ .

The resonance frequency shift at a bias flux of  $0.25 \Phi_0$  (Fig. 5.13) is 30 MHz, which is larger than the resonance line width of about 4 MHz. Hence, this scheme is capable of single-shot detection of the qubit flux state, which is going to be utilized in the next section for the qubit readout.

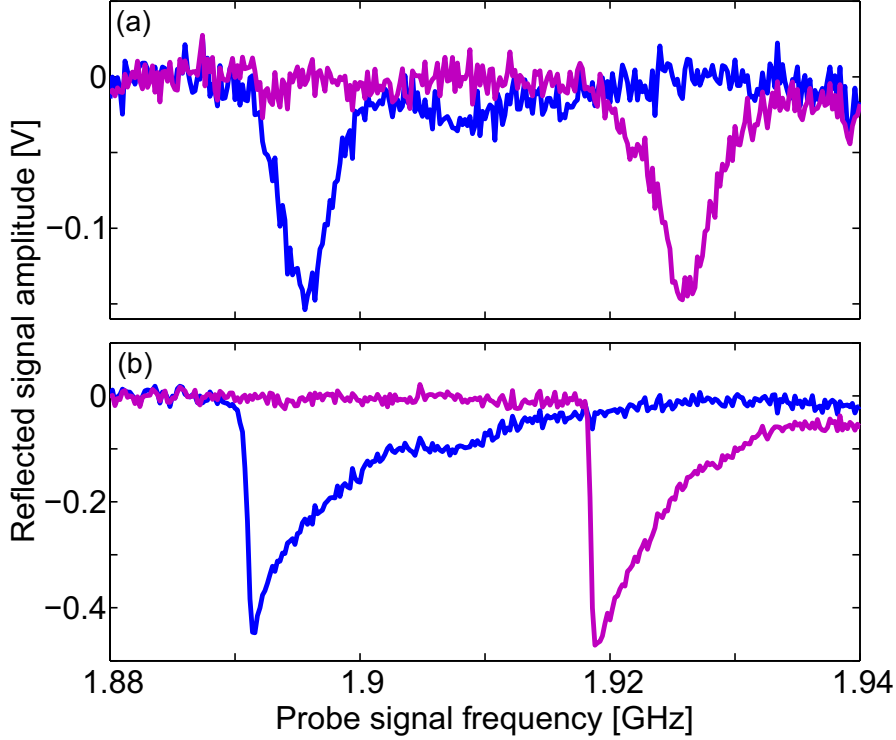


**Figure 5.15:** Shift of the resonance frequency of the SQUID resonator by 30 MHz due to the qubit changing its magnetic flux by approximately  $\Phi_0$ . (a) In the linear regime. (b) SQUID driven in the non-linear regime. Note the larger signal amplitude compared to the linear regime.

### 5.3.2 Qubit readout

After performing the measurements on the SQUID resonator in the frequency domain, to characterize the detector and to find the largest frequency shift, as the best working point for the qubit readout, we finally come to the actual measurements of the qubit itself. As already explained in section 5.2, the next measurement to do, is the qubit spectroscopy, to find the dependence of the qubit energy level splitting on the applied magnetic flux. Figure 5.16 shows the measured spectroscopy data of the qubit, acquired with the dispersive readout scheme, discussed in this thesis.

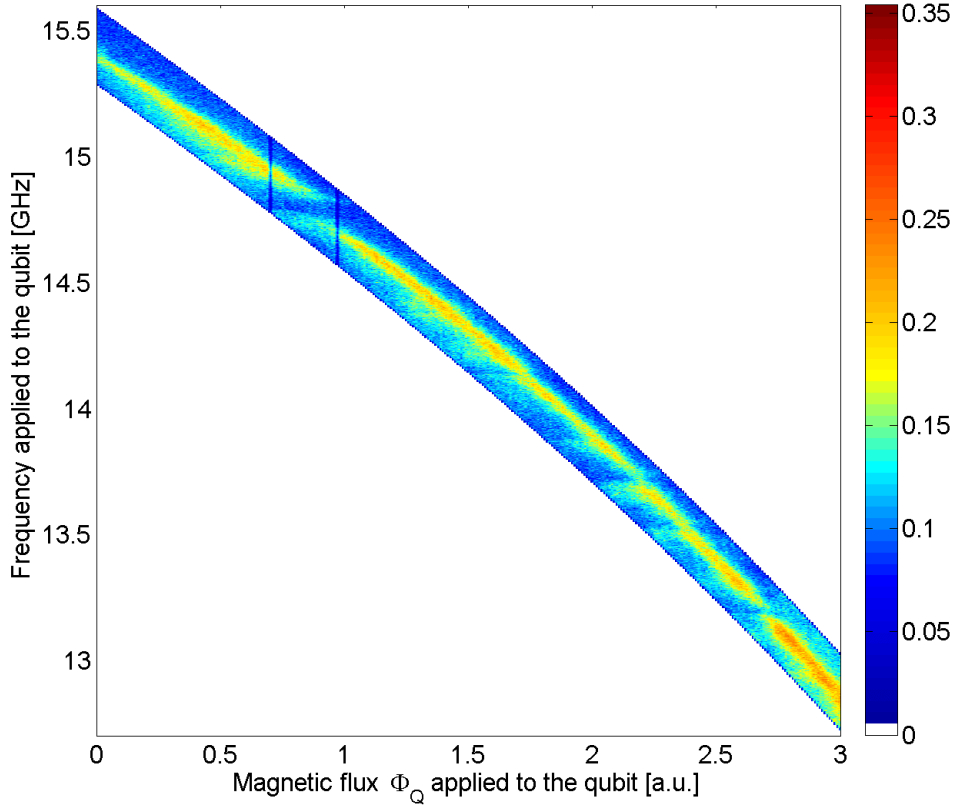


**Figure 5.16:** Qubit spectroscopy data. The probability of the qubit to be in the excited state, measured as the escape probability from the shallow potential well is shown here color encoded, versus the applied qubit bias flux [a.u.] on the horizontal axes, and the microwave frequency applied to the qubit on the vertical axis.

To demonstrate the successful implementation of the dispersive readout scheme for a Josephson phase qubit, we finally measured coherent oscillations between the first excited and the ground state of the qubit. Figure 5.17 shows Rabi oscillations of the qubit measured for different driving powers of the qubit microwave. As expected, the frequency of Rabi oscillations increases approximately linearly with the driving field amplitude.

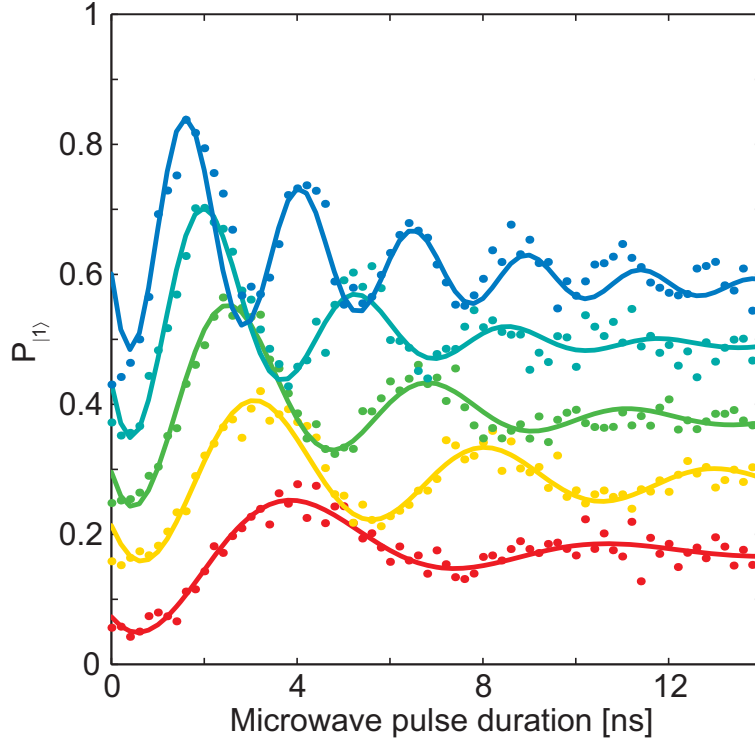


**Figure 5.17:** Coherent oscillations of the qubit for different driving powers, from bottom to top: -18 dBm, -15 dBm, -12 dBm, -9 dBm and -6 dBm. Curves are offset by 0.1 for better visibility.

The measured energy relaxation time of the tested qubit is rather short and on the order of  $T_1 = 5$  ns. This time is not limited by the chosen type of readout, but rather determined by the intrinsic coherence of the qubit itself. This is verified by measuring the same qubit with the conventional SQUID switching current method, which yields very similar  $T_1$ . The observed short coherence time is likely to be caused by the dielectric loss in the silicon oxide forming the insulating dielectric layer around the qubit Josephson junction [LLA<sup>+</sup>07].

## Conclusions

In this thesis a new type of readout for a Josephson phase qubit is presented. Instead of relying on the dissipative switching current measurement of a dc-SQUID and its disadvantages, to detect the flux states of the phase qubit, we make use of the Josephson inductance of the dc-SQUID. This flux dependent, non-linear inductance, together with an on-chip capacitor, is formed into a resonator circuit with a flux dependent resonance frequency around 2 GHz. By measuring the amplitude and phase of a microwave pulse reflected from the SQUID resonator, the flux state of the qubit is detected.

For this goal, a microwave setup including cabling, attenuators, filters and a cryogenic circulator, was planned according to the experimental needs and the restrictions predetermined by the installation in a dilution refrigerator at temperatures as low as 30 mK. For the room temperature microwave electronics, a custom made microwave board has been designed and assembled, containing, among other parts, a phase shifter, mixers for pulsing the probe signal, an optimized chain of amplifiers and, as a key element, an IQ-mixer to determine the amplitude and phase of the probe signal. A new broad band data acquisition card has been brought into operation to record the measurement data with sufficiently high speed, to fulfill the requirement of a high repetition rate. The dc-electronics have been improved to fulfill the needs of the faster measurement, e.g. a shorter rise time of the qubit flux bias current sources.

Additionally, low temperature laser scanning microscopy (LTLSM), a versatile technique that allows for the determination of the optical, dc- and microwave properties of an investigated device at the same time, was used for a first characterization of the resonators.

In conclusion, we have demonstrated a dispersive readout scheme for a Josephson phase qubit which was the goal of the presented research. This scheme avoids the switching of the SQUID flux detector into the resistive state. Due to much lower dissipation in the circuit, we can reduce the SQUID measurement time down to  $25 \mu\text{s}$  without observing any noticeable heating effects. This readout repetition time is about 40 times shorter than the time typically achieved with the conventional readout. In our setup, the shortest repetition time is limited by the amplifiers for the  $I$  and  $Q$  signals and could be further reduced down to the 10 - 100 nanosecond range by expanding the band of these amplifiers, as it has been already demonstrated for flux qubits [LSP<sup>+</sup>07]. This short measurement time and the possibility of using frequency-division multiplexing readout [MHI<sup>+</sup>08] make our approach promising for future experiments scaled up to multiple phase qubits.

Depending on the applied microwave power, the SQUID resonator circuit can be operated in either linear or nonlinear regime. The nonlinear regime allows for the use of extremely sensitive bifurcation readout [VDS09]. This may give rise to the possibility of direct quantum non-demolition readout of a Josephson phase qubit similar to what has already been realized for a flux qubit [LSP<sup>+</sup>07].

# Bibliography

- [AB63] V. Ambegaokar and A. Baratoff, *Tunnelling between superconductors*, Phys. Rev. Lett. (1963), 486.
- [Aer] Aeroflex / Inmet Inc., 300 Dino Drive, Ann Arbor, MI 48103 U.S.A., <http://www.aeroflex-inmet.com>.
- [BCS57] J. Bardeen, L. N. Cooper, and J. R. Schrieffer, *Theory of Superconductivity*, Phys. Rev. **108** (1957), 1175.
- [Bla66] A. Blaquière, *Nonlinear System Analysis*, Academic Press, New York, 1966.
- [BXR<sup>+</sup>03] A. J. Berkley, H. Xu, R. C. Ramos, M. A. Gubrud, F. W. Strauch, P. R. Johnson, J. R. Anderson, A. J. Dragt, C. J. Lobb, and F. C. Wellstood, *Entangled Macroscopic Quantum States in Two Superconducting Qubits*, Science **300** (2003), 1548–1550.
- [CB04] J. Clarke and A. I. Braginski (eds.), *The SQUID Handbook*, Wiley-VCH, Weinheim, Germany, 2004.
- [CFHB07] J. Claudon, A. Fay, E. Hoskinson, and O. Buisson, *Nanosecond quantum state detection in a current-biased dc SQUID*, Phys. Rev. B **76** (2007), 024508.
- [CNW98] J. C. Culbertson, H. S. Newman, and C. Wilker, *Optical probe of microwave current distributions in high temperature superconducting transmission lines*, Journal of Applied Physics **84** (1998), 2768–2787.

## BIBLIOGRAPHY

---

- [CSM<sup>+</sup>04] K. B. Cooper, M. Steffen, R. McDermott, R. W. Simmonds, S. Oh, D. A. Hite, D. P. Pappas, and J. M. Martinis, *Observation of Quantum Oscillations between a Josephson Phase Qubit and a Microscopic Resonator Using Fast Readout*, Phys. Rev. Lett. **93** (2004), 180401.
- [CTDL77] C. Cohen-Tannoudji, B. Diu, and F. Laloë, *Quantum Mechanics*, vol. 1, Wiley-Interscience, 1977.
- [Eme] Emerson & Cuming, 46 Manning Road, Billerica, MA 01821 U.S.A., <http://www.emersoncuming.com>.
- [FLS94] R. P. Feynman, R. B. Leighton, and M. Sands, *The Feynman lectures on Physics. 3: Quantum Mechanics*, Addison-Wesley, New York, 1994.
- [IOI<sup>+</sup>03] E. Il'ichev, N. Oukhanski, A. Izmailkov, T. Wagner, M. Grajcar, H.-G. Meyer, A. Y. Smirnov, A. Maassen van den Brink, M. H. S. Amin, and A. M. Zagoskin, *Continuous Monitoring of Rabi Oscillations in a Josephson Flux Qubit*, Phys. Rev. Lett. **91** (2003), 097906.
- [Jos62] B. Josephson, *Possible new effects in superconductive tunneling*, Phys. Lett. **1** (1962), 251.
- [KO11] H. Kammerlingh-Onnes, Leiden Comm. **120b**, **122b**, **124c** (1911).
- [Lik86] K. K. Likharev, *Dynamics of Josephson junctions and circuits*, Gordon and Breach Science, 1986.
- [Lis03] J. Lisenfeld, *Probing quantum states of Josephson junctions by microwaves*, Diploma thesis, Universität Erlangen-Nürnberg, 2003.
- [Lis08] J. Lisenfeld, *Experiments on superconducting Josephson phase quantum bits*, Ph.D. thesis, Friedrich-Alexander-Universität, Erlangen-Nürnberg, 2008.

- [LLA<sup>+</sup>07] J. Lisenfeld, A. Lukashenko, M. Ansmann, J. M. Martinis, and A. V. Ustinov, *Temperature Dependence of Coherent Oscillations in Josephson Phase Qubits*, Phys. Rev. Lett. **99** (2007), 170504.
- [LmcVS<sup>+</sup>04] A. Lupaşcu, C. J. M. Verwijs, R. N. Schouten, C. J. P. M. Harmans, and J. E. Mooij, *Nondestructive Readout for a Superconducting Flux Qubit*, Phys. Rev. Lett. **93** (2004), 177006.
- [LSP<sup>+</sup>07] A. Lupascu, S. Saito, T. Picot, P. C. de Groot, C. J. P. M. Harmans, and J. E. Mooij, *Quantum non-demolition measurement of a superconducting two-level system*, Nat Phys **3** (2007), 119–125.
- [LU08] A. Lukashenko and A. V. Ustinov, *Improved powder filters for qubit measurements*, Review of Scientific Instruments **79** (2008), 014701.
- [Luka] A. Lukashenko, Idea and design, Universität Erlangen-Nürnberg (2005).
- [Lukb] A. Lukashenko, Design and fabrication, Universität Erlangen-Nürnberg (2005).
- [Lup05] A. Lupaşcu, *Inductive readout for a superconducting flux qubit*, Ph.D. thesis, TU Delft, 2005.
- [McC68] D. E. McCumber, *Effect of ac Impedance on dc Voltage-Current Characteristics of Superconductor Weak-Link Junctions*, J. Appl. Phys. **39** (1968), 3113.
- [MDC85] J. M. Martinis, M. H. Devoret, and J. Clarke, *Energy-level quantization in the zero-voltage state of a current-biased Josephson junction*, Phys. Rev. Lett. **55** (1985), 1543.
- [MHI<sup>+</sup>08] J. A. B. Mates, G. C. Hilton, K. D. Irwin, L. R. Vale, and K. W. Lehnert, *Demonstration of a multiplexer of dissipationless su-*

## BIBLIOGRAPHY

---

- perconducting quantum interference devices*, Applied Physics Letters **92** (2008), 023514.
- [MNA<sup>+</sup>03] J. M. Martinis, S. Nam, J. Aumentado, K. M. Lang, and C. Urbina, *Decoherence of a superconducting qubit due to bias noise*, Physical Review B (Condensed Matter and Materials Physics) **67** (2003), 094510.
- [MNAU02a] J. M. Martinis, S. Nam, J. Aumentado, and C. Urbina, *Rabi Oscillations in a Large Josephson-Junction Qubit*, Phys. Rev. Lett. **89** (2002), 117901.
- [MNAU02b] J. M. Martinis, S. Nam, J. Aumentado, and C. Urbina, *Rabi Oscillations in a Large Josephson-Junction Qubit*, Phys. Rev. Lett. **89** (2002), 117901.
- [MOL<sup>+</sup>99] J. E. Mooij, T. P. Orlando, L. Levitov, L. Tian, C. H. van der Wal, and S. Lloyd, *Josephson Persistent-Current Qubit*, Science **285** (1999), 1036–1039.
- [NC93] H. S. Newman and J. C. Culbertson, *Measurement of the current-density distribution in high-temperature superconducting microstrip by means of kinetic-inductance photoresponse (invited paper)*, Microwave and Optical Technology Letters **6** (1993), 725–728.
- [NPT99] Y. Nakamura, Y. A. Pashkin, and J. S. Tsai, *Coherent control of macroscopic quantum states in a single-Cooper-pair box*, Nature **398** (1999), 786–788.
- [PDP<sup>+</sup>06] T. A. Palomaki, S. K. Dutta, H. Paik, H. Xu, J. Matthews, R. M. Lewis, R. C. Ramos, K. Mitra, P. R. Johnson, F. W. Strauch, A. J. Dragt, C. J. Lobb, J. R. Anderson, and F. C. Wellstood, *Initializing the flux state of multiwell inductively isolated Josephson junction qubits*, Phys. Rev. B **73** (2006), 014520.

- [Sch97] V. V. Schmidt, *The Physics of Superconductors*, Springer, 1997.
- [SKD<sup>+</sup>10] M. Steffen, S. Kumar, D. DiVincenzo, G. Keefe, M. Ketchen, M. B. Rothwell, and J. Rozen, *Readout for phase qubits without Josephson junctions*, Applied Physics Letters **96** (2010), 102506.
- [Spe] Spectrum Control Inc., 8031 Avonia Rd, Fairway, PA 16415 U.S.A, <http://www.spectrumcontrol.com>.
- [Ste68] W. C. Stewart, *Current-Voltage Characteristics of Josephson Junctions*, Appl. Phys. Lett. **12** (1968), 277.
- [SVP<sup>+</sup>04] I. Siddiqi, R. Vijay, F. Pierre, C. M. Wilson, M. Metcalfe, C. Rigetti, L. Frunzio, and M. H. Devoret, *RF-Driven Josephson Bifurcation Amplifier for Quantum Measurement*, Phys. Rev. Lett. **93** (2004), 207002.
- [VDS09] R. Vijay, M. H. Devoret, and I. Siddiqi, *Invited Review Article: The Josephson bifurcation amplifier*, Review of Scientific Instruments **80** (2009), 111101.
- [Whi] Whiteley Research Inc., 456 Flora Vista Avenue, Sunnyvale CA 94086, U.S.A, <http://www.wrcad.com>.
- [Wir06] T. Wirth, *Coupled Josephson phase qubits*, Diploma thesis, Friedrich-Alexander-Universität, Erlangen-Nürnberg, 2006.
- [WLC<sup>+</sup>03] A. Wallraff, A. Lukashenko, C. Coqui, A. Kemp, T. Duty, and A. V. Ustinov, *Switching current measurements of large area Josephson tunnel junctions*, Review of Scientific Instruments **74** (2003), 3740–3748.
- [YHC<sup>+</sup>02] Y. Yu, S. Han, X. Chu, S.-I. Chu, and Z. Wang, *Coherent Temporal Oscillations of Macroscopic Quantum States in a Josephson Junction*, Science **296** (2002), 889–892.

## BIBLIOGRAPHY

---

- [ZST<sup>+</sup>06] A. P. Zhuravel, A. G. Sivakov, O. G. Turutanov, A. N. Omelyanchouk, S. M. Anlage, A. Lukashenko, A. V. Ustinov, and D. Abraimov, *Laser scanning microscopy of HTS films and devices (Review Article)*, *Low Temperature Physics* **32** (2006), 592–607.
- [ZUHA02] A. P. Zhuravel, A. V. Ustinov, K. S. Harshavardhan, and S. M. Anlage, *Influence of LaAlO<sub>3</sub> surface topography on rf current distribution in superconducting microwave devices*, *Applied Physics Letters* **81** (2002), 4979–4981.

## List of publications

1. Microwave readout scheme for a Josephson phase qubit.  
T. Wirth, J. Lisenfeld, A. Lukashenko, and A. V. Ustinov.  
*Appl. Phys. Lett.* **97**, 262508 (2010).
2. A superconducting  $180^\circ$  hybrid ring coupler for circuit quantum electrodynamics.  
E. Hoffmann, F. Deppe, T. Niemczyk, T. Wirth, E. P. Menzel, G. Wild, H. Huebl, M. Mariani, T. Weiß, A. Lukashenko, A. P. Zhuravel, A. V. Ustinov, A. Marx, and R. Gross.  
*Appl. Phys. Lett.* **97**, 222508 (2010).



# Acknowledgements

I would like to express my sincere gratitude to all people who made this work possible and contributed to it in various ways.

First of all, I cordially thank my doctoral adviser Prof. Dr. Alexey V. Ustinov for giving me the opportunity to contribute to this very interesting field of research. I am very grateful for the experience and the knowledge I gained during my time in his group of international scientists. Moreover, I would like to thank Alexey for invitations to ski seminars and hiking, as well as climbing tours. I very much appreciate these "extracurricular" group activities and the nice memories related to them.

I am also very grateful to Dr. Jürgen Lisenfeld who introduced me to this exciting field of research already during my diploma work. Throughout my doctoral work, he has been a very knowledgeable "source" of useful hints, especially related to the measurement software as well as the setup. Thank you Jürgen for all your support in the past years.

Especially, I would also like to thank Dr. Alexander Lukashenko and Dr. Alexey Feofanov, for reliably helping me to maintain our dilution cryostats during my experiments. Sasha, I very much appreciate your vast amount of knowledge on low temperature setups and your hints on fitting them into the cryostat. Lyosha, I very much appreciate, you accompanying me throughout my time in the group, as well as the constant supply of "Eclaires" for the afternoons. Thank you to both of you for innumerable Ukrainian and Russian anecdotes that made live in the group even more enjoyable.

For nice, as well as helpful discussions about all interesting topics I would like to thank my fellow PhD students, Markus Jerger, Jochen Zimmer and Kirill Fedorov, sharing the office with me, as well as Dr. Hannes

## *Acknowledgements*

---

Rotzinger.

I am very grateful to Dr. Alexander Zhuravel for introducing me to the versatile technique of low temperature laser scanning microscopy.

I very much appreciate the effort of Dr. Stefano Poletto and Susanne Butz, they put in maintaining our coffee machine to keep it up and running.

Special thanks go to my "fellow Franconian", former Diploma student and good friend, Christian Schwemmer.

To all members of the group, both, former and current, I would like to express my gratitude for their cooperation and the friendly atmosphere they created.

I thank the whole "Karlsruhe team", represented here by Prof. Dr. Georg Weiß, Dr. Christoph Sürgers, Dr. Gerda Fischer, Steffi Baatz, Birgit Schelske and Lars Behrends, the electronic workshop, lead by Roland Jehle, the mechanical workshop, lead by Reinhold Dehm, and Franz Hartlieb, running the Helium liquifier, for all their support, before, during and after the move of the group, including the whole lab, from Erlangen to Karlsruhe in Summer 2008.

Moreover I would like to thank Prof. Dr. Paul Müller and Christa Metze from Physikalisches Institut III, standing here for all members of my former institute in Erlangen.

Especially I thank my best friend Axel for all his "non-physics input" into my life.

Last, but not least I want to thank my girlfriend Verena, my sister Bettina, my mum Marianne, my dad Herbert, and Barbara for giving me all imaginable support, trust and love throughout my studies and all of my life.